Fall 2014

Experimental investigation of the pebble bed structure by using gamma ray tomography

Fadha Shakir Ahmed

Department:

EXPERIMENTAL INVESTIGATION OF THE PEBBLE BED STRUCTURE BY USING GAMMA RAY TOMOGRAPHY

FADHA SHAKIR AHMED

A THESIS

Presented to the Faculty of the Graduate School of the
MISSOURI UNIVERSITY OF SCIENCE AND TECHNOLOGY

In Partial Fulfillment of the Requirements for the Degree of

MASTER OF SCIENCE IN NUCLEAR ENGINEERING

2014

Approved by:

Dr. Muthanna Al Dahhan

Dr. Gary Mueller

Dr. Hyoung-Koo Lee

ABSTRACT

Pebble Bed Reactors offer a future for new nuclear energy plants. They are small, inherently safe, and can be competitive with fossil fuels. The fuel forms a randomly stacked pebble with non-uniform fuel densities. The thermal-mechanical behavior of pebble bed reactor core is depends strongly on the spatial variation of packing fraction in the bed and in particular on the number of contacts between pebbles, and between the pebbles and the blanket walls. To investigate these effects, experimental data to characterize bed structure are needed along with other numerical simulation and computational tools for validation.

In this study, a powerful technique of high-energy gamma-ray computed tomography (CT scanner system) is employed for the first time for the quantification of the structure of pebble bed in term of the cross-sectional time-averaged void and distributions, it radial profiles and the statistical analysis. The alternative minimization (AM) iteration algorithm is used for image reconstruction. The spatial resolution of the CT scan is about 2 mm with 100×100 pixel used to reconstruct the cross-sectional image. Results of tomography with this advanced technique on three different pebble sizes at different axial levels are presented. The bed consisted of a glass spheres (Marbles) with a diameter d_1= 1.27 cm, d_2= 2.54 cm and d_3= 5 cm in a Plexiglas cylinder with diameter D = 30.48 cm (D/d_1 = 24, D/d_2 = 12 and D/d_3 = 6), and had an average void fraction $\bar{\varepsilon}_1$= 0.389, $\bar{\varepsilon}_2$ = 0.40 and $\bar{\varepsilon}_3 = 0.43$, respectively. The radial void fraction profile showed large oscillations with the bigger pebble diameters and the void fraction is higher on the wall with a minimum void fraction of 0.33 at 0.68 pebble diameter away from the wall. It was found that the void distribution in random packed bed depends strongly on the pebble diameter with respect to the bed diameter (D/d_p) and the packing mode. The oscillation is quiet large with the smaller aspect ratio (D/d_p) and decreases as the aspect ratio increases (D/d_p). It has been shown that increasing the bed height has no influence on the radial void fraction at the three levels of the bed. It can be seen that there is an agreement between the experimental results and the exponential expression model at the smaller sphere diameter (D/d_p=24). Comparison between the experimental and calculated methods were presented and discussed.

ACKNOWLEDGMENTS

I would like to express my gratitude to my supervisor, Prof. Al Dahhan for his guidance, valuable advice and encouragement during my master studies. He provided me with many opportunities that influence my career significantly. I appreciate his understanding and patience to finish this thesis. I would also wish to thank Dr. Mueller for the great assistance he provided at all levels of the research project. I would like to thank the other member of my committee, Dr. Lee for his strong support and research directions.

Special thanks to Dr. Rajneesh Varma (from Shell Oil Company) for his great help with CT operation and data processing. I would like to thank Dr. Pablo Vasquez for his assistance with the 3D image.

I would like to acknowledge the Department of Chemical and Biological Engineering & the Department of Nuclear Engineering, faculty, staff & Grad Students. My graduate experience benefitted greatly from the courses I took and the high-quality seminars that both departments organized.

I must thank all of the good friends, graduate and undergraduate students, officemates, and colleagues who have crossed paths with me over the years.

Most importantly, I am grateful to my family, wife and kids, for always being loving and supportive during my study.

Finally, I would like to acknowledge the US Department of Energy (DOE) Nuclear Energy Research Initiative (NERI) project (NERI-08-043) for the funding support to pursue research of this thesis.

TABLE OF CONTENTS

LIST OF FIGURES

LIST OF TABLES

NOMENCLATURE

I	radiation intensity (counts/s)
I_o	initial radiation intensity (counts/s)
μ_{eff}	effective mass attenuation coefficient ($g^{-1}cm^2$)
μ	linear attenuation coefficient (cm^{-1}) or mean in the statistical section
μ_s	attenuation coefficient through solid
μ_g	attenuation coefficient through gas
A	total attenuation
ρ	density (g cm^{-3}); ρ_s for solid & ρ_g for gas
L	length through the object (cm)
l_s	length through solid (cm)
l_g	length through gas (cm)
d_{eff}	special resolution (mm)
d_a	detector collimator slit width (mm)
S	source width (mm)
M	magnification factor
ε_g or ε	porosity (void fraction)
ε_s	solid fraction (solid holdup)
E	photon energy (eV)
H	Plank's constant ($6.626*10^{-34}$ Joule)
λ	wavelength (nm) or statistical parameter
C	speed of light (m/s)
λ_d	decay constant
N	number of atoms at time t
N_0	number of atoms at time t_0,
P	Probability
N	number of particles in the sample
X	Variable
M	Mean

σ	standard deviation
D	column diameter (cm)
d_p or d	particle diameter (cm)
r	radial position (cm)
R	radius of the column (cm), R_o: outer radius and R_i: inner radius
h	Cylinder or bed height (cm)
$\varepsilon(r)$	Radial void fraction
Np	Number of sphere particles
R_s	Sphere radius
r_s	Sphere center radial position

1. INTRODUCTION

1.1 OVERVIEW

There is an enormously higher demand of energy world-wide as a result of the significant world's population growth which is expected to be 10 billion people in the coming decades together with an increase of the living standards of the developing countries [1]. By far, the main energy sources are fossil fuels (oil) which has obvious concern on the global climate change. The striking feature is that oil is running out and there is a need of energy supply that is realistic to overcome the crisis of global warming under the condition of energy demand increase. Nuclear energy, which is a nearly carbon-free source of energy, could play an important role in reducing global greenhouse gas emission. A one Giga Watt nuclear plant can avoid about 6-7 million tons of CO_2 per year and related pollutants as compared to a coal-fired plants. There are about 440 nuclear power reactors in operation worldwide, providing approximately 16% of global electricity generation and almost one third of the European electricity production [2]. Reactors in operation around the world are generally considered as second or third generation systems, with most of the first-generation systems having been retired some time ago. There are still a couple of problems facing nuclear energy and one of them is the safety aspect. The fear of an accident happening either because of human error or due to a natural calamity is large. In conventional nuclear power plants, safety can be assured by adding appropriate safety systems. However, such systems are expensive and require highly skilled personnel. The cost of the safety systems provided added incentives to build larger reactors to reduce the cost of nuclear power per unit of electrical output. The IV generation reactors tries to solve some of these problematic issues by develop inherently safe nuclear reactors. The Generation IV International Forum (GIF) was initiated in 2000 and formally chartered in mid-2001. It is an international collective representing government of 13 countries where nuclear energy is significant now and also seen as vital for the future. Most are committed to joint development of the next generation of nuclear technology. Generation IV International Forum (GIF) is founded on several technology goals that include improving nuclear safety, improving proliferation resistance, minimizing waste and natural resource utilization, and decreasing the cost to

build and run such plants [3]. Generation IV International Forum has identified six preferred reactor concepts for commercial deployment about the year 2030. The Very High Temperature Reactor (VHTR) is one of six advanced concepts chosen by the US Department of Energy (DOE) for further research and development under the Generation IV program. VHTR is a graphite-moderated, helium-cooled reactor with a once-through uranium fuel cycle. It supplies heat with high core outlet temperature (~750-1000 °C) which enables applications such as hydrogen production or process heat for the petrochemical industry or others [4]. At the present, two fuel types were proposed for the VHTRs core, the pebble bed reactor (PBR), such as the Chinese HTR-10, and the prismatic block type fuel reactor, such as the Japanese HTTR. PBR is a promising type of the high temperature gas cooled reactor whose distinguishing feature is the spherical fuel elements consisting of coated particles of uranium dioxide fuel embedded in a graphite matrix, while the prismatic type fuel consists of several columns of stacked prismatic blocks. These blocks are hexagonal graphite blocks that are arranged side-by-side in a honeycomb configuration and then stacked vertically in columns to create the core. The nuclear fuel particles are in a form of pellet stacked on the top of each other in fuel channels where the helium passes through other cooling channels to remove the heat.

1.2 PEBBLE-BED REACTOR

In pebble-bed reactors the fuel is contained in pebbles of graphite rather than in metallic rods which are used in reactors like the Boiling Water Reactor (BWR) and Pressurized Water Reactor (PWR). The graphite pebbles of typically 60 mm in diameters contain about 5000 to 20,000 coated TRISO particles. These TRISO particles contain a fuel kernel of UO_2. The structure of the fuel spheres is shown in Figure 1.1. The pebble-bed reactor has two major benefits. The first one is that the reactor can be cooled with an inert gas like helium. An inert gas is not reactive under normal circumstances and the gas does not get radioactive as fast as water, which is used in conventional Light Water Reactor (LWR). However, with the high working temperature of the reactor, the energy conversion efficiency improve**s.** The other major advantage is that it is extremely unlikely that it will ever suffer a catastrophic melt down at high temperatures.

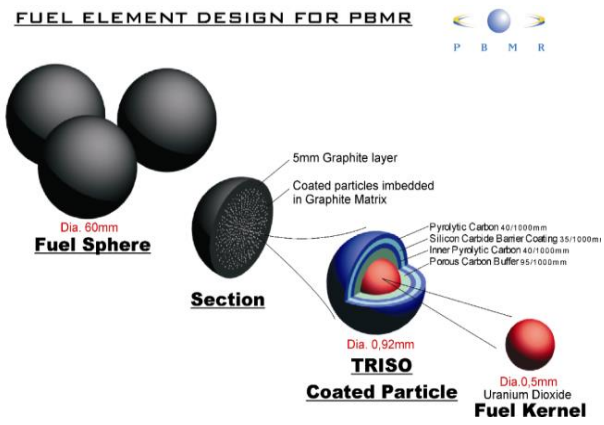

Figure 1.1: Pebble-bed reactor fuel containing TRISO coated particles in a graphite matrix fuel surrounded by a 0.5 cm graphite shell [5]

The low power density and high temperature resistance of the core materials ensure that any decay heat will be dissipated and transported to the environment without the decay heat causing a meltdown. Figure 1.2 shows the sketch of the pebble-bed reactor [6]

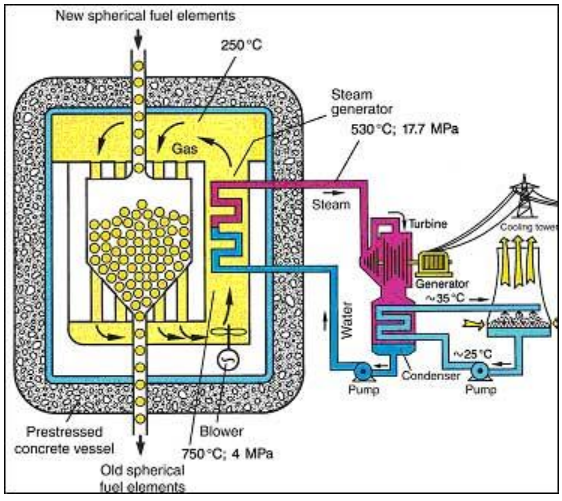

Figure 1.2: Sketch of pebble-bed reactor

The pebbles in PBRs are inserted randomly in the reactor core to form packed pebble-bed. The pebble bed reactor continuously recirculates the fuel spheres using an on-line refueling system. A slow continuous down flow of pebbles goes through the reactor core while the reactor is operating. Pebbles are continuously added at the top of the core and removed at the bottom. The pebbles pass through the reactor core several times before being fully spent. Extracted pebbles are sent through a burnup-determining radiation detector that either sends the pebble to discharge and to be replaced with a new ones or recycles it back to the core for additional burnup. This enables the PBRs to operate with very low excess nuclear reactivity and relatively low enrichments. Graphite pebble is flowing in the core of the bed as moderation while fuel pebbles flow in the surrounding region. A schematic diagram of the refueling system is shown in Figure 1.3.

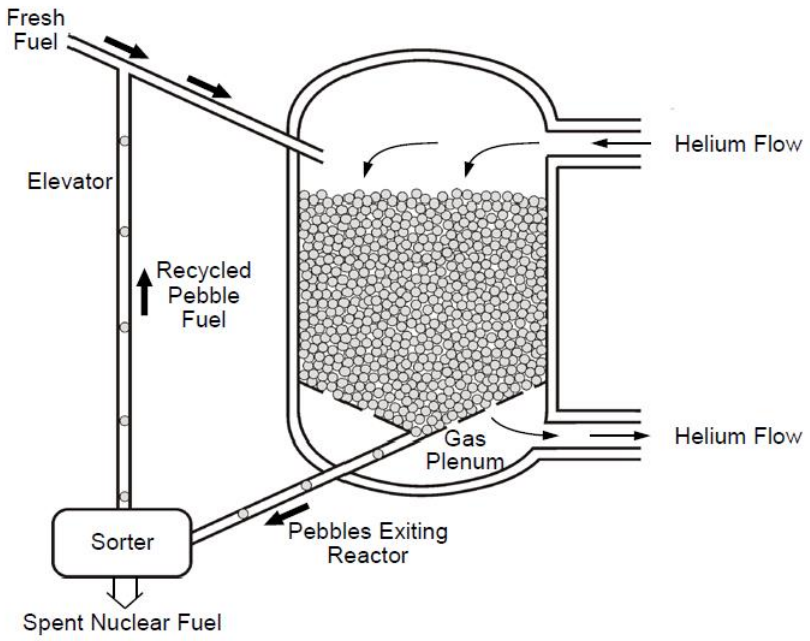

Figure 1.3: Online refueling schematic in a gas cooled PBR [5]

1.3 MOTIVATION

The mechanisms of fluid (helium gas) flow and heat transfer in such bed are sensitive to the axial and radial void volume fraction distribution (porosity) [7]. The dynamic of the pebble flow is poorly understood and the bed structure has not been studied properly. However, it has been reported in the literature for small particles beds that the porosity in packed beds varies periodically from the wall. This has a major impact on the reactor physics. In addition, proper input of the bed structure (void and solids distribution) to computational fluid dynamics (CFD) codes is the key for proper prediction of the CFD as the fluids in packed beds follow the least resistance path represented by high void volume fraction. However, such structure has not been studied experimentally in details. This can be studied experimentally using advanced imaging technique such as X-ray and gamma-ray tomography to measure the cross-sectional, radial distribution holdup profiles and their statistical analysis in the pebble beds. Tomography has found widespread application in many scientific fields, including medicine, physics, chemistry, astronomy, geophysics, and engineering. Although X-ray CT has a good spatial resolution in a small-scale object, it is not preferentially used in industrial applications due to their lower energy and limited penetration. In contrast, gamma-ray tomography is widely used in a large scale and high-density object in industry because of their higher energy and penetration power [8]. Usually, phase holdup distribution images are obtained by determining the attenuation values of the individual phases in the system by using gamma scanner and a suitable imaging reconstruction process. In this study, the dual energy-dual source computed tomography (DE-DSCT) scanner was used to measure the void and solids fractions cross-sectional distribution and the radial profiles at different heights using different pebble sizes.

1.4 OBJECTIVES

The overall objective is to advance the understanding of the pebble bed structure in terms of voids and solids cross-sectional distribution and radial profiles along the bed height using gamma ray computed tomography (CT) (DE-DSCT). The CT measurements will be first validated against phantom represents multi-phase object. Furthermore, the experimental results are used to assess the predictions of the reported empirical and

analytical correlations. The experimental results obtained will be used to demonstrate a 3D image of the entire bed with quantitative information about axial and radial void fraction distribution.

1.5 THESIS ORGANIZATION

A general review of pebble bed structural studies, and available correlations and experimental methods to determine solids and void fraction distribution is provided in Chapter 2. The DSCT facility, experimental setup, the experimental conditions and the validation of CT scanner are discussed in chapter 3. Pebble bed structure characterization will be explained in chapter 3. In chapter 4 a comparison of experimental and calculated void fractions using the selected reported correlations is presented followed by 3D visualization of the inner bed structure. The conclusion of this work and future direction of research in imaging the pebble bed reactor are discussed in Chapter 5.

2. LITERATURE REVIEW

In this chapter, a literature review pertinent to this thesis is presented. It is divided into two parts. In the first part, experimental use of gamma ray tomography is briefly reviewed. The second part reviews in more details the bed structure characterization studies in pebble packed beds using experimental, empirical, analytical and computational methods.

2.1 GAMMA RAY TOMOGRAPHY

Many non-destructive gamma ray (CT) experimental studies on bed structure characterization and multiphase flow measurements have been made during the last decades from different points of view (Aboulwafa and Kendal [9], Harrison [10], Bowman [11], Kumar [12], Kumar et al., [13], Chaouki et al., [14], Roy [15], Chen et al., [16], Wang et al., [17], Rados [18], Roy et al., [19], Rados et al., [20], Hampel [21], Varma [22], Vasquez [23], AlMesfer [24] and Ahmed [25]. Gamma ray computed tomography has been successfully used to determine the radial void fraction of the pebble bed reactors. Dijk [26] used an Am-241 gamma source tomography experiment to investigate the void fraction distribution and wall channeling effects in an acrylic cylinder with one foot height and 9 inch in diameter. The facility used to be a scale down model of the HTR-10 which is currently active in China. Auwerda et al. [27] performed radial void fraction measurements in pebble bed reactor with cylinder to pebble diameter ratio (D/d = 18) using a computational tools and experimental gamma tomography to validate these tools. The results showed good agreement for the Discrete Elements Method (DEM) and expanding system method with the experiment for both average and radial void fraction. More details about gamma ray tomography concept and usage will be found in chapter 3.

2.2 PACKING STRUCTURE INVESTIGATION IN PEBBLE BEDS

2.2.1 Experimental Studies. Pebble bed nuclear reactors are one of the promising types of the 4^{th} generation nuclear energy that are under development. They contain large numbers of spherical graphite pebbles with fuel elements inside and graphite pebbles as moderator. These fuel pebbles are very slowly cycled through the nuclear core in a dense granular down flow. The pebble bed is cooled by concurrently down flow of helium which enters at about 500 ºC and leaves the bed at ~ 900 ºC or

higher. Hence, the pebble bed reactor can be considered as a packed bed compared to the flowing gas [28]. The design of a pebble bed is based upon mechanisms of heat and mass transfer, and the flow and the pressure drop of the fluid (helium gas) through the bed of solids. These mechanisms are influenced by the void fraction (porosity) of the packed bed and it may lead to a non-uniform temperature distribution at the reactor wall and the outlet of the pebble bed due to the sharp varies of porosity from the wall to the bed center. The knowledge of the packing structure and flow patterns of pebbles in the pebble bed is thus important to any study of the transport phenomena in the reactor core as well as safety assessment [29]. Among in-core fuel cycle studies that require the knowledge of the packing distribution are the macroscopic transport and diffusion data, fuel depletion prediction, and pebble bed densification [30]. In addition, in recent increasing use of the Computational Fluid Dynamics (CFD) it becomes necessary to know the positions of all particles in the bed to simulate the fluid flow inside the reactor. The minimum bulk porosity of a uniform size spheres packing is about 0.36 and the typical rang of porosity values reported in the literature fall between 0.36 and 0.42 [31]. These literatures reported a significant variation in the void fraction in radial direction. They found that the porosity at the wall was 1.0 and that it decreased to a minimum value of about 0.25 at a distance of approximately 0.5 sphere diameters from the wall. The porosity then oscillated through maximum and minimum before settling out to the bulk porosity at a value of approximately 0.39. Spheres near a container wall form more ordered structures than spheres in the internal region of random packing due to a significant fraction between the particles in contacting with the container wall, which leads to alignment on a cylindrical surface. The second layer of spheres will tend to lodge themselves in the deepest pockets formed by the wall spheres creating a less organized structure. The wall effect will disappear a few sphere diameters into the packing [31]. The void fraction fluctuations from the wall inwards depends on the aspect ratio (bed diameter to particle diameter, D/d), method of charging (loading pattern) and the shape of particles.

Over the years several experiments have been performed to measure void fractions in cylindrical packed beds of mono size spheres using destructive and non-destructive techniques. Early experiments of Roblee et al. [32] and Benenati and Brosilow [33],

liquid wax and epoxy resin were used to fill the interstices of spheres packed bed (D is 1.62 inch, d_p are 0.622, 0.29, 0.115, 0.08 and D/d_p are 2.61, 5.6, 14.1, 20.3). Upon curing of the wax or resin, the solid cylinder was machined in stages to successively smaller diameters and the weight and diameter of the cylinder was measured after each machining. In this manner the mean density of each annular ring removed could be measured and the void fraction could be determined. These experiments showed that the radial porosity presents large fluctuation near the cylinder wall that dampens out at about three to five sphere diameters from the wall towards the packed bed center. Goodling et al. [34] used a plastic cylindrical packed bed filled with a polystyrene spheres (D/d are 7.78, 7.4, 8.41, 8.56, 10.7, 16.8). The void then filled with a mixture of epoxy and finely ground iron particles. Annular rings were then cut from the outer periphery and the bed was weighted and the void was measured. They found that the porosity is approached unity at the wall and then oscillated in a damped fashion toward the bed center. Kufner and Hofman [35] used a resin to fill the void between the particles in a fixed bed (D are 20 & 42 mm, d are 3.5 & 4.5 mm with D/d ratio of 4-12). The tube was cut into layers and the cuts were polished. Photographs were taken of these cuts and analyzed with image analyzer. From these data, an average radial porosity distribution could be measured. Mueller [36] measured the center position coordinates of specially prepared Plexiglas spheres with small steel spheres at their centers in randomly packed fixed bed using X-ray radiography (D are 25.75, 50.5, 76.00, and 101.88, d is 12.75 and D/d are 2.02, 3.96, 5.96 and 7.99) . The radial void fraction distribution was then determined from these center coordinates. Niu et al. [37] used the X-ray computed tomography to analyze the radial porosity distribution in a bed of randomly packed uniform spheres (Dc = 5, 7, 10 cm and d_p = 1 cm). Sederman et al. [38] used a magnetic resonance imaging technique (MRI) to study the porosity distribution in the radial direction in cylindrical packed beds of balloting spheres filled with water (D is 27 mm, d_p are 3, 1.9, 1.4 and D/d are 9, 14, 19). The results from these experimental works observed oscillations in the porosity distribution in the radial direction which were in good agreement with those obtained by other investigators. A procedure similar to that employed by Goodling et al [34] was followed by Toit [29] to calculate experimentally the radial variation of porosity in a packed bed consisted of 3.6 mm lead balls at a bed of 50.4 mm in diameter. The

experimental results were compared with those obtained from the analysis of numerically packed beds. The results show the same damped oscillatory behavior in the variation of porosity in the radial direction ranging from a maximum at the wall to the bulk value in the pebble bed center. Hassan et al. [39] used the particle tracking velocimetry (PIV) and refractive index matching techniques to present a flow structure in a pebble bed reactor. Mariani et al. [40] used a cylindrical bed (D are 10.72 cm and 6 cm) packed with uniform size polypropylene spheres (d are 2.5 cm and 1.19 cm). X-ray computed tomography (CT) was used to determine the position of each sphere center, then to evaluate the packing properties at local and global scales. Experimental results from two aspect ratios D/d (4.92 and 5.04) were analyzed and quantitatively compared to the simulated packed beds with a good agreement. Auwerda et al. [27] developed a non-destructive method using gamma-ray scanning to measure void fractions (absolute and radial void fraction profile) in a randomly stacked pebble bed (D is 2.29 cm, d is 1.27 cm and D/d is 18.0). The results were used to validate three different computational tools. The radial void fraction profile showed large, dampened oscillations near the wall extending up to five pebble diameters into the pebble bed, with a minimum void fraction of 0.22 half a pebble diameter away from the wall. The computational methods generate the pebble beds with void fraction in a good agreement with the experimental values.

It is obvious from above that all the studies reported in the literature and derived correlations for void fraction prediction were performed using much smaller particle sizes than the size of the typical pebbles. This necessitates the need to conduct studies on quantifying the bed structure using relatively large particle sizes which is the focus of this study.

2.2.2 Correlations for Calculating the Average Void Fraction in Pebble Beds. The mean void fraction for spheres in cylinders packed beds have been investigated by many authors using various empirical correlations based on experimental and analytical methods. The average void fraction in pebble bed reactor is a statistical characteristic of the bed which is required for thermal and hydraulic of contact and adsorption vessels. It depends on many factors such as the method of charging/discharging, the shape of particles and the aspect ratio (cylinder to particle diameter ratio or D/d_p). The void fraction of a fixed bed can be determined

experimentally from the total density of the bed (ρ_T) and the density of packed particles (ρ_s):

$$\varepsilon = 1 - (\frac{\rho_T}{\rho_s}) \quad \text{..... (1)}$$

Correlations proposed for average void calculation as a function of the aspect ratio (D/d) produce considerable differences even for the same cylinder to particle diameter ratio due to the random and disordering in packed bed structure.

Jeschar [41] and kugeler et al. [42] both calculated the average bed porosity using the following formula:

$$\varepsilon = 0.375 + 0.34\frac{d_p}{D} \quad \text{..... (2)}$$

The standard correlation for predicting overall void fraction in a packed bed of spheres was developed by Dixon [43] and is reproduced by Theuerkauft et al. [44]:

$$\varepsilon = 0.4 + 0.05\frac{d_p}{D} + 0.412\left(\frac{d_p}{D}\right)^2 \quad \text{..... (3)}$$

De Klerk [45] proposed the following equation to describe the void fraction in a packed bed with small aspect ratio:

$$\varepsilon = 0.41 + 0.35e^{-0.39\frac{D}{d}} \quad \text{..... (4)}$$

Pushnov [46] derived an empirical expression to calculate the void fraction of a bed of spherical particles for ratios *D/d* less than 2.4:

$$\varepsilon = 12.6(D/d)^{6.1}e^{-3.6(D/d)} \quad \text{..... (5)}$$

$$\varepsilon = \frac{1}{(D/d)^2} + 0.375 \quad \text{for D/d > 2 and h>20 } d_p \text{.....(6)}$$

Another correlation is proposed by Zou & Yu [47]

$$\varepsilon = 0.372 + 0.002\left[e^{\left(\frac{15.306}{D/d_p}\right)} - 1\right] \quad \text{..... (7)}$$

Mueller [36] proposed an empirical correlation to calculate the bed porosity (ε_b) in a cylinder packed bed of spheres:

$$\varepsilon_b = 0.365 + \frac{0.22}{D/d} \quad \text{..... (8)}$$

Sodre and Paris [48] proposed that the value of average porosity for an annular bed (at annulus) is given by:

$$\bar{\varepsilon} = 0.3517 + 0.387\frac{d_p}{2(R_o - R_i)} \quad \text{..... (9)}$$

Where R_o is outer radius of annulus and R_i is the inner radius of the annulus.

Finally, an exponential expression to determine the average bed porosity in packed bed of monosized spheres was proposed by Ribeiro et al. [49]. This expression is suitable for random dense packing and for $2 \leq \frac{D}{d_p} \leq 19$ and is given by:

$$\epsilon = 0.373 + 0.917e^{(-0.824\frac{D}{d_p})} \quad \text{..... (10)}$$

2.2.3 Correlations for Calculation the Radial Voidage Variation in Pebble Beds. In the core of the pebble-bed reactor there are two types of pebbles in pebble beds, namely graphite and fuel pebbles. The graphite balls fill the cylindrical center of the pebble bed and fuel balls surround the graphite balls. Both the graphite and the fuel pebbles are extracted from the bottom and reinserted (or replaced in case of burn up) on the top of the pebble-bed. This extracting and reinserting gives rise to a pebble velocity of about 4.5(mm/h) [50]. Since this flow is slow we can approximate the pebble bed as a fixed packed bed. As mentioned earlier, the determination of void fraction distributions in pebble bed is highly important to the mechanisms of heat and mass transfer and also flows and pressure drop of the coolant throughout the pebble bed. Because of the sensitivity of those mechanisms to the void fraction it becomes important to know the void distribution inside the pebble-bed and knowledge of the porosity is necessary for any rigorous analysis of the transport phenomena in the bed [34]. The geometry in the packing of a pebble-bed is interrupted at the wall and this gives rise to large void fraction variations near the wall. The flow through a medium depends on this porosity and because of the wall disturbance in the void fraction profile of the pebble-bed the velocity

profile (of the cooling gas) is also disturbed. This phenomenon is called wall-channeling [51]. By researching the wall channeling effect, a better void fraction profile can be obtained and this knowledge can lead to better and more efficient pebble bed reactors.

In the past three decades, many empirical correlations and analytical and computational methods to describe the packing structure in packed beds and PBRs have been proposed by various researchers. The void fraction data of Benenati and Brosilow (1962) [33] for uniform spherical particles have the typical oscillatory variation in void fraction in the region of the wall. Different spheres diameters were studied in their experiment with a tube diameter of 1.624 inch and D/d_p equal to 2.61, 5.6, 14.1, and 20.3 respectively (d_p = 0.62, 0.29, 0.115 and 0.08 inch) . An empirical fit of these data is shown in Equation (11)

$$\varepsilon(x) = 0.38 + 0.62e^{-1.7x^{0.434}}\cos(6.67x^{1.13}) \quad \text{(11)}$$

where x is the number of d_p from the wall and equal to $(1-\xi)\delta/2$, ξ is a dimensionless radial coordinate (r/R) and δ is radial aspect ratio (R/R_p). They presented results for a number of cases with D/d varying from 2.6, 5.6 and larger.

Martin [52] proposed the following correlation based on experimental data of Benenati and Brosilow [33]:

$$\varepsilon(x) = \begin{cases} \varepsilon_{min} + (1-\varepsilon_{min})x^2, & -1 \le x \le 0 \\ \varepsilon_b + (\varepsilon_{min} - \varepsilon_b)e^{-\frac{x}{4}}\cos\left(\frac{\pi}{C}x\right), & x \ge 0 \end{cases} \quad \text{(12)}$$

With $$X = 2\frac{R-r}{d_p} - 1 \quad \text{(13)}$$

$$C = \begin{cases} 0.816 & \frac{D}{d_p} = \infty \\ 0.876 & \frac{D}{d_p} = 20.3 \end{cases} \quad \text{(14)}$$

The minimum void fraction is in the range of ε_{min}=0.20-0.26 and ε_b is the bulk void fraction not affected by wall effect (near the bed center).

Cohen and Metzner [53] used a quantitative description of void variations reported in the literature to describe the oscillatory variation of void away from the wall using the following set of correlations:

$$\frac{1-\varepsilon(x)}{1-\varepsilon_b} = 4.5\left[x - \frac{7}{9}x^2\right] \qquad for\ x \le 0.25 \quad \text{(15)}$$

$$\frac{\varepsilon(x)-\varepsilon_b}{1-\varepsilon_b} = a_1 e^{(-a_2 x)} cos[a_3 x - a_4]\pi \qquad for\ 0.25 < x < 8 \quad \text{(16)}$$

$$\varepsilon(x) = \varepsilon_b \qquad for\ 8 \le x \le \infty \quad \text{(17)}$$

$$x = \frac{R-r}{d_p} \quad \text{(18)}$$

The constants are (a_1=0.3463; a_2=0.4273; a_3=2.4509 and a_4=2.2011) with D/d_p range from 7 – 60.

The void fraction distribution in a fixed packed bed with spheres is modeled using an exponential type function similar to the form proposed by Vortmeyer and Schuster [54], Cheng and Hsu [55] and white and Tien [51]. The latter proposed radial void distribution for an annular packed bed of the form:

$$\varepsilon(r) = \frac{1}{\left[1+\left(\frac{1-\varepsilon_b}{\varepsilon_b}\right)\sqrt{1-e^{\left(-2\frac{r-R_i}{d_p}\right)}}\right]} \qquad for\ R_i \le r \le \frac{R_0+R_i}{2} \quad \text{(19)}$$

$$\varepsilon(r) = \frac{1}{\left[1+\left(\frac{1-\varepsilon_b}{\varepsilon_b}\right)\sqrt{1-e^{\left(-2\frac{R_0-r}{d_p}\right)}}\right]} \qquad for\ \frac{R_0+R_i}{2} \le r \le R_0 \quad \text{(20)}$$

An empirical correlation has been determined by Mueller [36] for the radial void fraction distribution using his experimental results (Mueller 1992) and other existing data for d_p = 1.27 cm and different D diameters (2.57, 5, 7.6, and 10.1 cm):

$$\varepsilon(r) = 0.365 + \frac{0.22}{D/d_p} + \left(0.635 - \frac{0.22}{D/d_p}\right) J0\left(a\frac{r}{d_p}\right) e^{\left(-\frac{0.315r}{d_p}+\frac{0.725r}{D}\right)} \qquad for\ 2.02 \le D/d_p$$

(21)

where *J0* is Bessel function of the first kind of order zero

$$a = \begin{cases} 7.45 - \frac{3.15}{\frac{D}{d_p}} & for\ 2.02 \le D/d_p \le 13.0 \\ 7.45 - \frac{11.25}{\frac{D}{d_p}} & for\ 13.0 \ge D/d_p \end{cases} \quad \text{..…….. (22)}$$

Mueller 2010 [56] developed analytical and semi-analytical equations to estimate the radial porosity of spheres packed bed. These expressions accurately predicted the radial porosity in the near and far wall regions and is given by:

$$\varepsilon(r) = 1 - \sum_{n=1}^{Np} \frac{S_n(r)}{2\pi r h} \text{……..…….. (23)}$$

where *Np* is the number of sphere particles, $S_n(r)$ is the intersecting area of an nth-sphere at the radial position *r* and *h* is the bed height. $S_n(r)$ can be determined by applying the equation:

$$S_n(r) = \pi[R_s^2 - (r - r_s)^2]\ for\ R_s \le r_s \le R - R_s \quad with\ r_s - R_s \le r \le r_s + R_s \text{ (24)}$$

Where R_s is sphere radius and r_s is the sphere center radial position. The distribution of the sphere particle centers required to generate the void distribution is provided by Mueller model [36].

Computational methods to generate randomly packed pebble bed got more attention in the recent years. Toit [57] applied a Discrete Elements Method (DEM) to generate void fraction profiles to be used in the reactor thermal-hydraulics studies in pebble bed reactors. Salvat et al. [58] developed an algorithm to simulate the structure of packed beds of spherical particles of uniform size in cylindrical containers. Using DEM simulation, both Cogiliati [59] and Rycroft [60] simulated pebble flow in pebble bed reactors. Monte Carlo simulation has been applied by Kloosterman [61] to generate a packing pebble bed. Auwerda et al. [27] used experimental results to evaluate three different computational methods to generate randomly stacked pebble beds: DEM, Monte Carlo rejection method, and an expanding system method. They found that the numerical results were in a good agreement with experimental data. Mariani et al [40] analyzed the structure of packed bed of mono-sized spherical particles in cylinder using two tools (tomography and simulation). The algorithm used to simulate the bed structure is

rendering the position of each sphere in the container. The results from the simulation agree very well with the experimental profiles. A morphologic/topologic analytical tool was used by Pieritz et al. [62] to monitor the arrangement of pebbles in a pebble bed. The computational methodology was successfully applied to determine the radial and axial void fraction indicating a structured sphere arrangement in zones close to wall. A new method is established by Mueller [63] to examine the radial variation of void fraction in cylinders packed with mono-sized spheres. In his method the local radial porosity profiles can be easily formed for any axial location in pebble bed in addition to the axially averaged radial void fraction. The method is derived from geometrical and analytical techniques to determine the arc length-based radial porosity. More recently, Khane (2014) [64] performed a new integrated experimental and computational study of granular flow in PBR. He applied a (DEM) based simulations of test reactor geometry and validated simulation results with the experimental data. He found that static friction characteristics play an important role in packed bed structural characterization and suggested to add this parameter to existing empirical equations.

The above studies have clearly demonstrated that the void fraction distribution in a packed bed does depend on the size of the column which is basically increases with decreasing D/d_p ratio. The implication of these studies is that one should use large D/d_p ratios to reduce the wall-effect. Unfortunately, most of these studies were used a small columns, small particle sizes and small D/d_p ratios. It is therefore imperative to use lager columns and larger particles sizes to better understand the wall effect and to evaluate other computational and empirical methods.

3. EXPERIMENTAL WORK

3.1 OUTLINE OF THE EXPERIMENTAL SETUPS

The Dual Source Computed Tomography (DSCT) scanner facility has been established in one of the Professor Al-Dahhan's laboratories related to industrial imaging and visualization using radioisotopes based techniques at G2 Fulton Hall of Missouri S&T. The setup was made in such a way that measurements of the axial and radial void fraction profiles could be obtained. The DSCT scanner setup is shown in Figure 3.1.

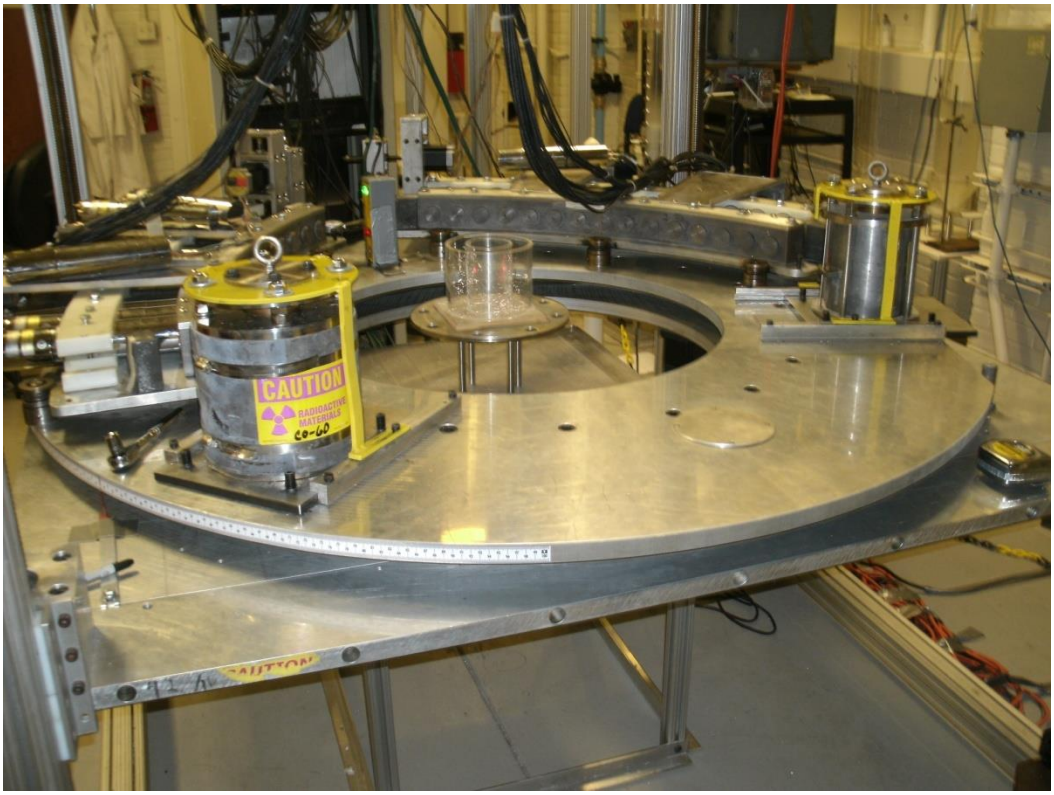

Figure 3.1: The gamma-ray DSCT measurement system

The CT scans were performed on the following experimental conditions:

a. A Perspex test phantom consisting of two circular sections of 3 and 6 inch diameters. The circular sections were filled with air and water for CT system validation.
b. A Plexiglas pebble bed reactor with outside diameter of 30.48 cm (12 in.) and a height of 30.48 cm (12 in.). The solids used in this study were glass spheres (Marbles) with three different mean diameters of 1.27 cm (0.5 in.), 2.54 cm (1 in.) and 5 cm (2 in.), as shown in Figure 3.2. In this experiment, three axial levels were scanned at heights of 7.62 cm (3 in), 15.24 (6 in.) and 22.86 (9 in.).

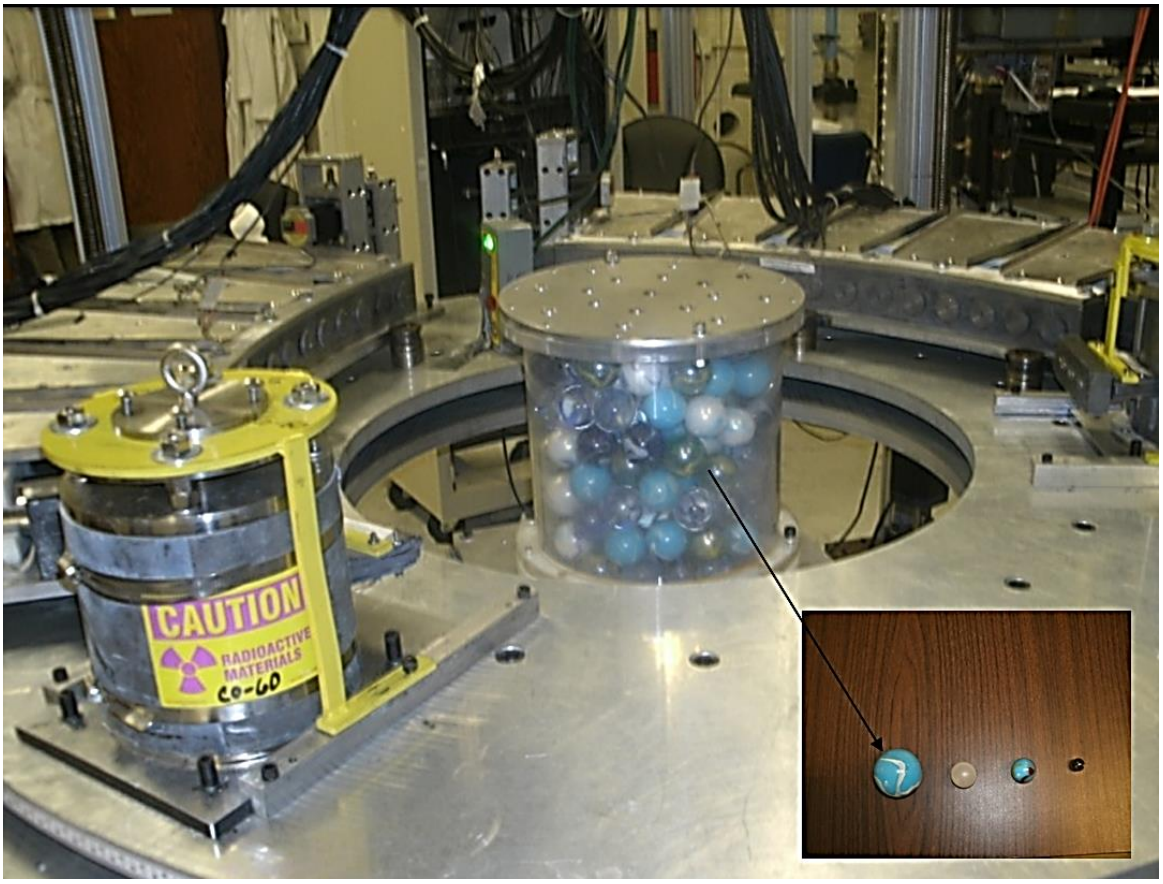

Figure 3.2: DSCT technique with a 12 inch setup pebble bed reactor of 2 inch pebbles

c. A Plexiglas pebble bed reactor with outside diameter of 30.48 (12 in) and a height of 30.48 (12 in). The solids used in this experiment were 1750 glass spheres of 1 inch in diameter (D/d=12). Twenty levels were used along the bed height with increment of 0.5 inch from the bottom of the bed.
d. A Plexiglas pebble bed reactor with outside diameter of 30.48 (12 in) and a height of 30.48 (12 in). One inch diameter solids used (D/d=12). In this experiment, only one level in the center has been scanned with two different packing modes.
e. A Plexiglas pebble bed reactor with outside diameter of 12 in. and a height of 24 in. The solids used in this experiment were 458 glass spheres with two inch in diameter (D/d=6). CT scans were performed at six elevations, 3, 6, 9, 15, 18 and 21 inch from the reactor base. Figure 3.3 shows the 2 feet pebble bed reactor filled with 2 inch Marbles.

The following are descriptions about CT, the related scanning steps and the validation of the technique using a phantom.

3.2 GAMMA RAY COMPUTED TOMOGRAPHY (CT)

3.2.1 Concept of Tomography. The science of tomography imaging stems from the fundamental property of any material to attenuate electromagnetic radiation of any wavelength as it passes through the material [65]. If the intensity of a beam of radiation incident on a body is I_o, and the intensity after the radiation passes through the body is I, then the attenuation function is defined as the ratio I/I_o. Invoking the dual particle and wave nature of electromagnetic radiation, attenuation refers to a decrease in the intensity of the incident radiation (decrease in number of photons) as the beam passes through the object of interest. Equivalently, since each photon is an independent entity, the attenuation function also reflects the "probability" that a photon entering the object of interest eventually leaves the object and continues on its path, without any interaction with the material of the medium. The attenuation of any beam of radiation depends on the property called "linear attenuation coefficient" (product of the mass attenuation coefficient, μ ($g^{-1}cm^2$) and density ρ ($g\ cm^{-3}$)), and is a function of the distance the beam traverses in the medium.

Figure 3.3: Setup of 2 feet pebble bed reactor filled with 2 inch pebble size mounted inside the DSCT technique

Thus, a denser medium (such as a solid) attenuates more radiation (hence leads to a higher decrease of photon counts) while a lighter medium (such as a gas) causes less attenuation. Therefore, if the attenuation of a controlled beam of radiation by an intervening medium can be quantified or measured, then this information can be used to back-calculate the density of the medium. The above description is shown schematically in Figure 3.4. It can be shown mathematically [65] that if the fate of all photons is accounted for only by absorption, transmission or scattering (i.e. all photons are conserved, known as the "conservation of particles" law), then:

$$\frac{I}{I_\circ} = exp\left[-\int_{l(x,y)=0} f(x,y,z)ds\right] \ldots\ldots\ldots\ldots\ldots\ldots\ldots\ldots\ldots\ldots\ldots\ldots\ldots\ldots\ldots\ldots\ldots\ldots\ldots (25)$$

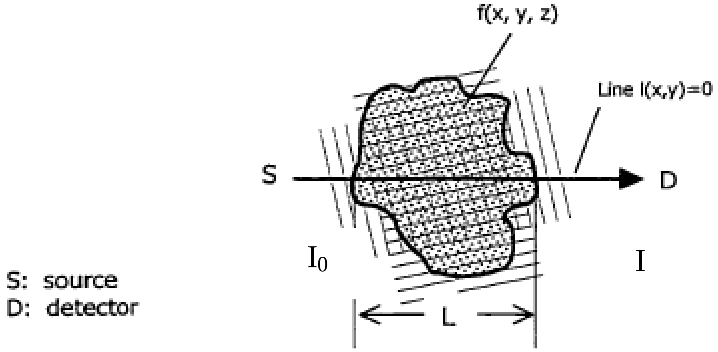

Figure 3.4: Attenuation of a beam of radiation by an intervening density distribution f(x,y,z)

Thus, the attenuation, measured in terms of the ratio between the measured intensity (photon counts, *I*) in presence of the intervening medium (of density distribution *f(x, y, z)*) to that incident intensity in free space (I_o), is simply the line integral of the density distribution measured along the line of the beam (of Equation (1) *(x, y) = 0*). The line integral, as the name implies, represents the integral of some parameter of the object along a line.

Beer and Lambert also came to the same conclusion based on purely empirical grounds, and their result is stated in the law that bears their name; the so called Beer-Lambert's law,

$$\frac{I}{I_\circ} = exp\left[-\int_{l(x,y)=0} \mu_{eff}ds\right] \ldots\ldots\ldots\ldots\ldots\ldots\ldots\ldots\ldots\ldots\ldots\ldots\ldots\ldots\ldots\ldots\ldots\ldots\ldots\ldots (26)$$

μ_{eff} is a point function and is referred to as the effective mass attenuation coefficient which is equivalent to $\mu\rho$ of the material. Mathematically μ_{eff} is equivalent to *f(x, y, z)* in

Equation (25), sampled along a line (chord) given by $l(x, y) = 0$. Using a single projection measurement (i.e., a single measurement of I and I_o along some chosen chord shown in Figure 3.5, it is possible to back-calculate the line-average of the μ_{eff} or $f(x, y, z)$ function if the chord length is known. This average, however, is taken along a single line and does not, in general, reflect the cross-sectional distribution $f(x, y, z)$. The tomography problem is an inverse problem to reconstruct the function $f(x, y, z)$ based on the measurements of the line-averages of attenuation along various chords in the object of interest (i.e. the family of lines given by $l_i(x, y) = 0$).

Tomography is the logic extension of the densitometry idea. In the densitometry, the attenuation measurement is made by placing the source and detector on either side of the object being scanned and moving the assembly so as to yield chordal averages of the density distribution (Figure 3.5). Tomography provides us with very powerful tools to recreate cross-sectional density distributions inside any kind of opaque system, which could be as varied as the human body, chemical reactors, or the earth's interior. Referring back to Equation (25), one may rewrite it for 2D as:

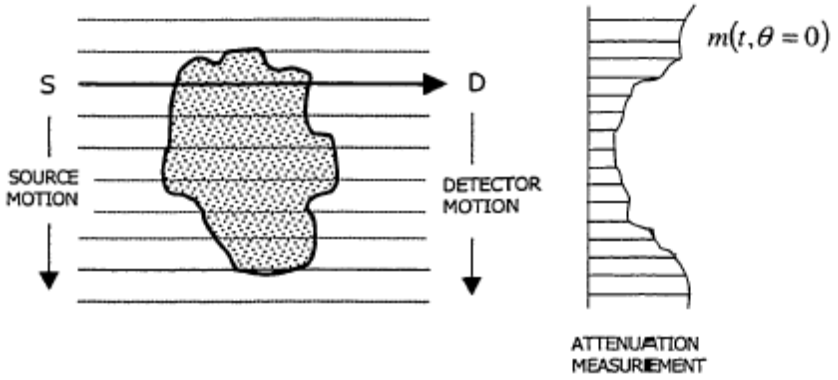

Figure 3.5: Schematic of a gamma ray densitometry

$$ln\left(\frac{I}{I_\circ}\right) = m(t,\theta) = \iint f(x,y)\delta(x\cos\theta + y\sin\theta - t)\,dxdy \quad \ldots\ldots\ldots\ldots\ldots\ldots\ldots\ldots (27)$$

where *m(t, θ)* refers to a single projection measurement which is obtained along the line whose equation is given for a more general case as follows and as shown in Figure 3.6 in which the beam at a certain angle *(θ)* with respect to the origin:

$$x cos\theta + y sin\theta = t \ldots\ldots\ldots\ldots\ldots\ldots\ldots\ldots\ldots\ldots\ldots\ldots\ldots\ldots\ldots\ldots\ldots\ldots\ldots\ldots\ldots\ldots\ldots \ldots\ldots\ldots\ldots (28)$$

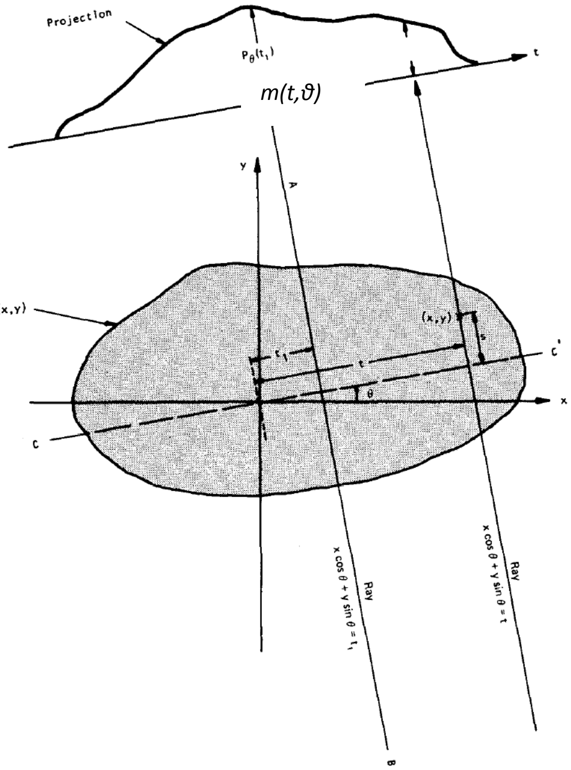

Figure 3.6: Geometrical configuration of a tomographic projection

It is to be noted here that for the special case shown in Figure 3.5 where *θ=0*, Equation (27) simplifies to the following form:

$$\ln\left(\frac{I}{I_\circ}\right) = m(t,\theta=0) = \iint f(x,y)\delta(x-t)dxdy \ldots\ldots\ldots\ldots\ldots\ldots\ldots\ldots\ldots\ldots\ldots (29)$$

The two-dimensional line integral in Equation (27) is clearly in the x-y space and has a non-zero value only along the line of the projection represented by Equation (28),

because of the presence of the two-dimensional Dirac delta function. A projection is formed by combining a set of line integrals. The simplest projection is a collection of parallel ray integrals as is given by $m(t, \theta)$ for a constant θ. This is known as a parallel projection and is shown in Figure 3.7. It could be measured, for example, by moving a source and a detector along parallel lines on opposite sides of an object. Then the process is repeated by varying θ. Another way to think about that is by considering the projection to be a transformation of the x-y domain to the t- θ domain. Thus one acquires a whole two-dimensional array of projections $m(t, \theta)$, and one is required to "re-construct" the 2D density distribution function $f(x, y)$ in Equation (27).

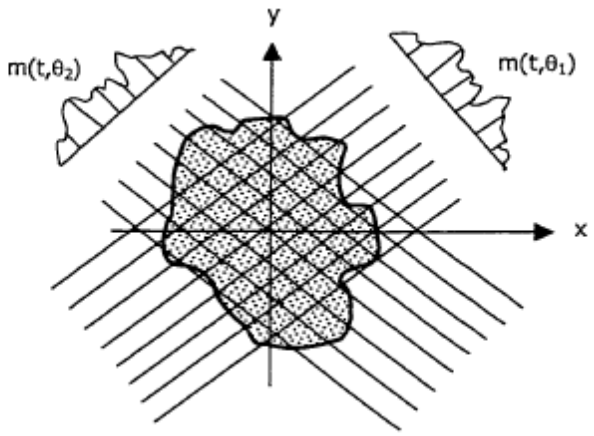

Figure 3.7: Tomographic scanning at different angular orientations (parallel projection)

Another type of projection is possible if a single source is placed in a fixed position relative to a line of detectors. This is shown in Figure 3.8 and is shown as a fan beam projection because the line integrals are measured along fans. To reconstruct the image given by sufficient number of projections, the Fourier Slice Theorem is used [65]. This theorem states that the single-dimensional Fourier transform of set of parallel projections through a two-dimensional transform $f(x, y)$ (i.e. the Fourier transform of $m(t, \theta)$ for a fixed θ), gives a slice of the two-dimensional transform $F(u, v)$ of $f(x, y)$

oriented at an angle θ in the u-v plane. This is given in Equation (30) below and shown schematically in Figure 3.9.

$$F(u,v) = \int_{-\infty}^{\infty}\int_{-\infty}^{\infty} f(x,y)e^{-j2\pi(ux+vy)}dxdy \quad \text{..... (30)}$$

The simplest example of the Fourier Slice Theorem is given for a projection at $\theta=0$. First, consider the Fourier transform of the object along the line in the frequency domain given by $v=0$. The Fourier transform integral now simplifies to

$$F(u,v) = \int_{-\infty}^{\infty}\int_{-\infty}^{\infty} f(x,y)e^{-j2\pi ux}dxdy \quad \text{..... (31)}$$

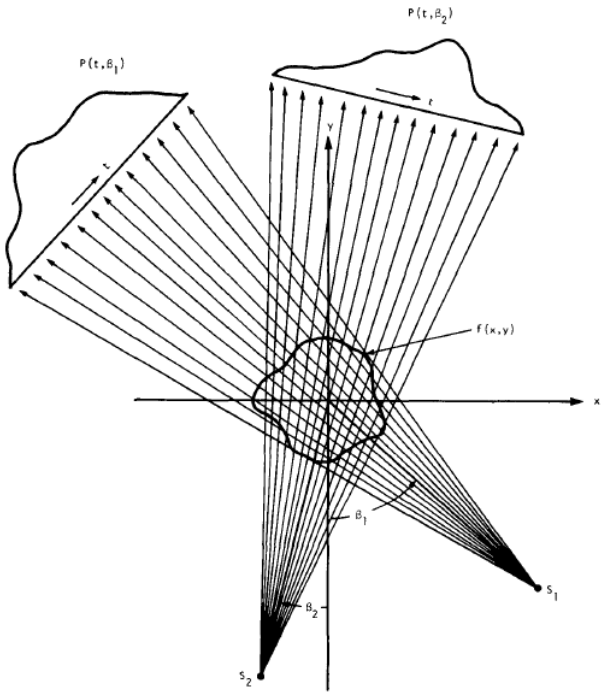

Figure 3.8: Fan beam projection [9]

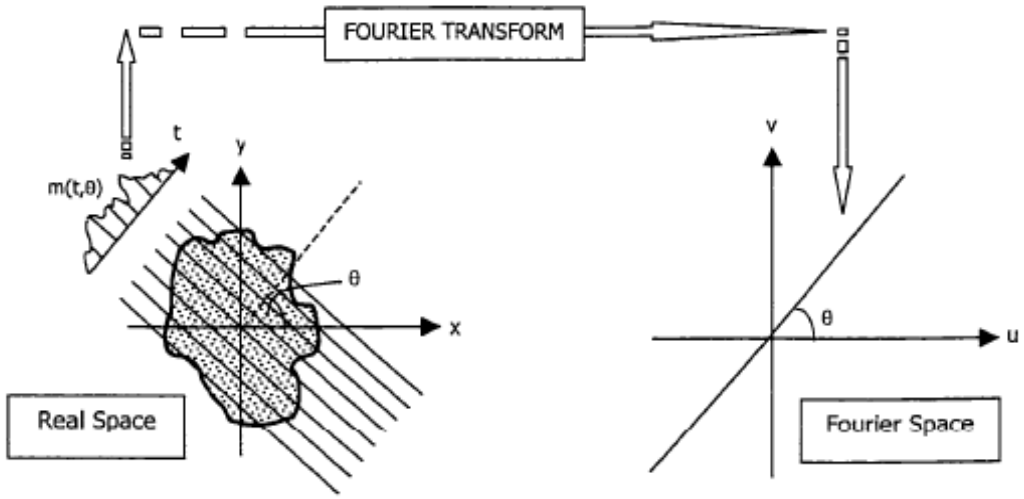

Figure 3.9: The Fourier Slice transfor

Thus, given the Fourier transform of a projection at enough angles the projections could be assembled into a complete estimate of the two-dimensional transform and then simply inverted to arrive at an estimate of the object. Figure 3.10 shows a typical result of that kind in which the dots represent the actual location of estimates of the object's Fourier transform.

3.2.2 Gamma Ray Tomography Importance and Applications. Although traditional methods based on the use of probes have the ability to provide data with fine time resolution, such probes are not only intrusive, but also need to be moved through the volume of the system being studied in order to map the entire flow field. Methods that have the ability to provide relevant measurements throughout the flow field without disturbing the flow are clearly advantageous. Gamma ray Computed Tomography (CT) is one such technique that is capable of providing the holdup distribution of phases in multiphase systems. The advantage of tomography lies in its noninvasiveness and in the ability to obtain the parameters of interest over an entire cross-section of the flow field of interest. The holdup and its distribution in a multiphase system are important in determining the interfacial area available for heat and mass transfer between the phases.

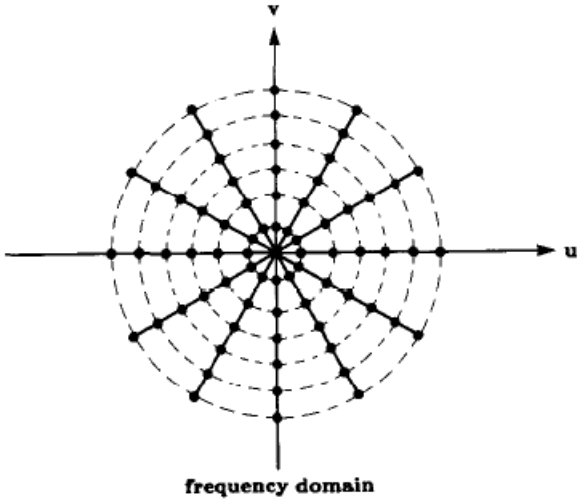

Figure 3.10: Projections collection in the Fourier space

Tomography has been in use in the medical field for diagnostic radiology for more than 70 years. However, the application of tomography to engineering applications is relatively recent (mid 1980's). Applications range from nondestructive testing of manufactured components, the investigation of process equipment (process tomography), to underground imaging in relation to environmental remediation of contaminated soil and groundwater etc. In the process industry, tomography aids in the characterization of flow in multiphase opaque reactors, which is essential in providing a proper basis for modeling their hydrodynamics and the reaction process involved. In these systems, the phases (especially the solid phase) involved are opaque and prevent the use of optical technique for the measurement of flow parameters. Thus, tomography in its various forms provides the only means to obtain the required information.

3.2.3 Gamma radiation statistics. Gamma radioactive isotopes decay to stable isotopes by emitting γ rays. Gamma rays are electromagnetic waves with frequencies between 10^{19} and 10^{21} *Hz* [66]. They are emitted spontaneously from an atomic nucleus during radioactive decay in packets referred to as photons. The energy transported by a photon is related to the wavelength λ or frequency υ by

$E = hv = hc/\lambda$……..……..……..… (32)

where *c* is the velocity of light, and *h* is Plank's constant ($6.626*10^{-34}$ Joule). The energy is expressed in eV (electron-volts). Each nuclear species (isotope) emits gamma rays of one or more specific energies. Activity, is the rate of radioactive decay and decreases exponentially according to

$Activity = \lambda_d N = \lambda_d N_0 e^{-\lambda dt}$……..……..…… (33)

where λ_d is the decay constant, and *N* and N_0 are the number of atoms at times *t* and t_0, respectively. The emission of radiation is a statistical process which is a very important aspect while measuring radiation. Counting statistics play an important role in the measurement of radioactive phenomena, which are random and discrete in nature. The radioactive decay of a nucleus is a statistical process which can be defined by Poisson distribution. The Poisson distribution is a simplified binomial distribution where there are very small probabilities, *p*, of individual observations (decay of one particle in our case) and a very large number, *n*, of observations (number of particles in the sample). The parameter $\lambda=np$ then occurs for a given variable, *X*, with the probability, $P(X; \lambda)$, can be defined by Poisson distribution,

$P(X;\lambda) = \left(\lambda^X e^{-\lambda}\right)/X!$……..... (34)

$P(X; \lambda)$ is the probability of observing *X* events when λ events are expected. If $\lambda >>1$, the Poisson distribution approaches a normal distribution (Figure 3.11) and is thus characterized by the mean, $\mu = \lambda$, and the standard deviation, σ. In this Figure, the red line illustrates the relative error decreasing exponentially with increasing count rate and also corresponds to the Poisson distribution for λ = X. The important point is that for binomial distributions σ is related to *m*, and for the Poisson distribution

$\sigma = \mu^{1/2}$……..……..… (35)

3.2.4 Types of Radioactive Isotopes Used for Gamma Ray Tomography. The two isotopes more frequently used in gamma tomography are ^{137}Cs and ^{60}Co. The ^{137}Cs is the source of choice for nuclear gauging applications in the industry as it has a long half life and emits single clean peak and don't have scatter interference of photons of other energies. ^{60}Co is the next best as the signal from the highest peak would not have any scatter interference. Since the second peak is close to the first, the scatter interference in signal is minimal. These two sources are very widely used in many industrial related

nuclear applications. The details of radioactive isotopes that can be used in gamma ray computed tomography are given in the Table 1 below. There are many factors that govern the selection of a radioactive source in gamma ray CT such as strength (activity), energy, half-life, cost, and radiation safety. The choice of radioactive source is primarily dependent on the materials and size of the object of interest to ensure a high penetration capability and less measurement error.

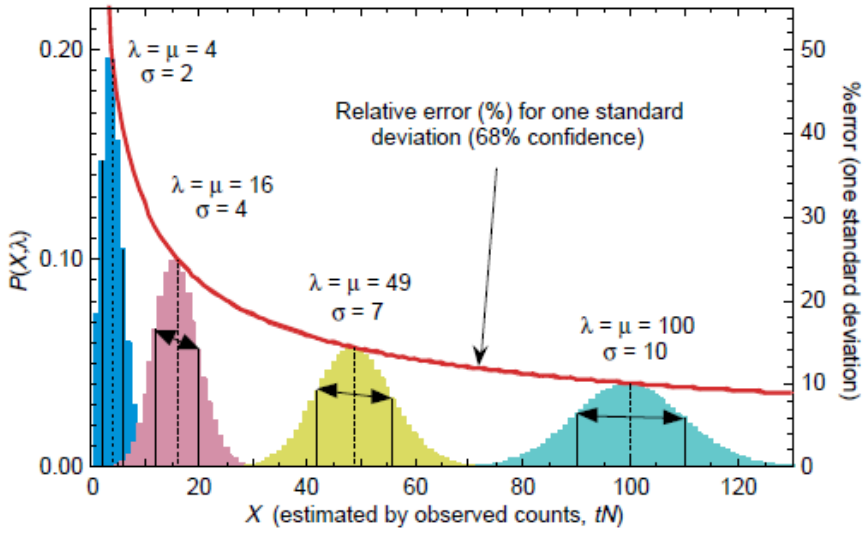

Figure 3.11: Poisson distributions for four selected lambda values. One-standard-deviation intervals are shown.

Table 3.1: Types of radioactive isotopes used in gamma tomography [67]

Isotope	Half Life	Type of Decay	Mass Excess (MeV)*	Major Radiations (MeV)	Principal Means of Production
$_{55}Cs^{137}$ Cesium	30.07 Years	β^-	-86.9	β^-: 1.175 (7%), 0.513 (95%) γ: 0.662 (85%)	La^{139}(n, α) Ba^{138}(d, α)
$_{27}Co^{60}$	5.27 years	β^-	-61.651	β^-: 1.49 (0.1%), 0.318 (100%)	Co^{59}(n, γ)

Table 3.1: Types of radioactive isotopes used in gamma tomography [67] (Cont.)

Cobalt				γ: 1.173 (100%), 1.332 (100%)	
$_{34}Se^{75}$ Selenium	120 days	EC	-72.166	β^-: 0.462 (96%), 0.584 (2.2%) γ: 0.265 (59%), 0.136 (58%), 0.280 (25%)	Se^{74}(n, γ) As^{75}(d, 2n)
$_{56}Ba^{133}$ Barium	10.5 years	EC	-87.67	γ: 0.0309 (65%), 0.0306 (35%) 0.035 (11.6%)	Ba^{133}(n, γ) Cs^{133}(p, n)
$_{63}Eu^{152}$ Europium	13.5 years	EC (72%), β^- (28%), β^+ (0.021%)	-72.89	β^-: 1.48 (8%), ε: 0.344 (25%) γ: 0.334 (26%), 0.121 (28.5%)	Eu^{151}(n, γ)
$_{70}Yb^{169}$ Ytterbium	32 days	EC	-60	γ: 0.197 (36%), 0.177 (22%), 0.11 (17.5%), 0.063 (44%)	Yb^{168}(n, γ) Tm^{169}(d, 2n)
$_{95}Am^{241}$ Americium	432 years	α and β stable	52.96	α: 5.48 (85%), 5.44(13%) γ: 0.059 (36%)	Daughter Pu^{241}

∗ The difference between its actual mass (in a.m.u.) and its mass number (*A*)

3.3 IMAGE RECONSTRUCTION PROCESS

There are basically two kinds of algorithms for an image reconstruction. One is a transformation based method such as Fourier Transform (FT), Back Projection (BP) and Filtered Back Projection (FBP), the other kind is an iterative reconstruction method such as Algebraic Reconstruction Technique (ART), Simultaneous Iterative Reconstruction Technique (SIRT), Expectation Maximization (EM) and Alternating Minimization (AM) [68]. Expectation maximization (EM) and alternating minimization (AM) algorithms have been greatly used to process gamma ray tomography data to image void and solids or gas, liquid and solids distribution in various multiphase systems. Both algorithms account for the stochastic nature of the gamma ray transmission across the domain of interest. This makes these algorithms more favorable for image reconstruction to determine the phase holdup distribution. The EM algorithm is an iterative algebraic technique used to find the maximum likelihood estimates from measured projections depends on distribution of attenuation coefficients across the domain. 'Each' iteration of

the EM algorithm consists of two steps: expectation (E step) and maximization (M step). The algorithm was first presented in the open literature for the first time for transmission tomography by Lange and Carson [69]. Details of principles and discussions of EM algorithm can be found at Dempster et al., [70], Kumar [12] and Roy [15].

The alternating minimization (AM) algorithm, formulated by O'Sullivan and Benac [71], is an iterative algorithm accounts for the stochastic nature of the gamma ray photons. In the AM algorithm, the maximum likelihood problem is formulated as a double minimization of an I-divergence to obtain a family of image reconstruction algorithms [72]. In the minimization process there is no approximation made as in the case of EM, which represents one of its advantages over the EM algorithm. A comparison study of EM and AM algorithms for single source gamma ray tomography can be found in Varma et al., [73]. The results show an overall improvement in the quality of the image in terms of the noise and accuracy of the estimated values when the AM algorithm is used to determine the holdup distribution images of the two phases in the phantoms. In the current study, AM algorithm has been used for all reconstruction images to characterize the pebble bed structure.

The reconstruction of the attenuation coefficients image from the raw scanned data is obtained in a stepwise process which involves:

- Averaging the raw data
- Calculating the transmission ratios
- Geometry input data - Calculating the length of the chords for each projection
- Assigning initial guess
- Image reconstruction using iterative algorithm (AM)
- Calculating the phase holdups
- Averaging and plotting data

In each step, a corresponding code is used. All these codes and computer programs are documented in Professor Al-Dahhan's Laboratory.

3.3.1 Outline of the Procedure to Obtain Cross Sectional Values of Void and Solids. The goal of implement CT technique is to obtain void and solids fractions distribution across the 2D domain for a fixed axial position. To achieve this goal, the following steps have to be taken:

a. CT scans

A complete set of CT experiments to obtain the phase density distribution in a reactor cross-section consists of scanning the actual experiments as well as several reference scans (e.g. empty column, column with one single phase like liquid or solid). The type of reference scans depends on the reactor system and the phases involved (either two or three phases). The sampling frequency is defined based on the magnitude of counts received by the detectors for each projection. In the pebble bed reactor the following conditions scans have to be performed.

- Only air in the path between source and the detectors (i.e., perform the scan without placing the object in CT)
- Column containing solids only (packed bed)

b. Averaging the raw data

The first step of reconstruction is to average the data points of each projection for each sampling period (Δt) and for all scans performed to reduce the effect of noise and uncertainty in the data and to get a better quality of the images. The mean value of the counts based on multiple samples or readings for a given projection is often used for processing the data.

c. Calculating transmission ratio and Sinogram

The averaged data files for both packed bed and air (without object) scans are used to calculate the transmission ratio (I/I_o) of the scanned section. The transmission ratio is the ratio of counts obtained while scanning the object to that obtained when only air is present (I/I_o). The sinogram tool has been implemented in this study to visualize the attenuation values for all positions of source and detectors. Sinogram can be used as a diagnostic tool to identify any error in the detectors or its electronics. Figure 3.12-(a) shows the Sinogram for the projection profile of packed bed with 0.5 inch marbles. In this figure, the projection number is shown in the Y-axis (315 projections) and the source position (view) is shown in the X-axis (197 views). The pixels in the Sinogram image (Figure 3.12-a) represent transmission ratio for each related view and projection. As can be seen, there is no artifacts (bands) in this image representing a typical good quality of the counting system. Figure 3.12-(b) shows a transmission ratio plot for 12 inch packed

bed (Y-axis) and the angular position of the projection in the fan beam with respect to the central beam of that view (X-axis). This plot should be smooth and symmetric along the center. It is always advisable to make such a plot as an intermediate step in the reconstruction to assess the correctness and quality of the scan. The all CT scans for the packed pebble bed should have the same typical good scan to obtain as shown in Figure 3.12.

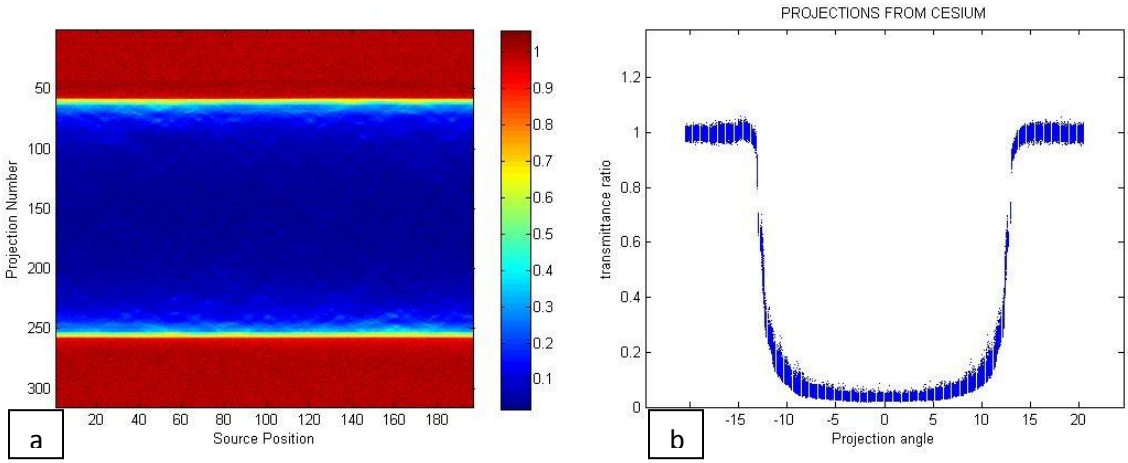

Figure 3.12: (a) The Sinogram of projection profile in a packed bed reactor- projection number versus source position (view) (b) The transmission ratio (I/I_0) for all 197 views of the packed bed

d. Computation of geometry input data for reconstruction

In the reconstruction, data obtained during scans are interpreted in terms of Beer-Lambert's law:

$$I = I_o \cdot exp(-\mu \cdot l) \quad \text{..... (36)}$$

where, in general, I_o is the incident radiation and I is the detected radiation intensity after passing through length l [cm] of object whose linear gamma-ray attenuation coefficient is μ (cm^{-1}). This equation is used to obtain the attenuation coefficient values from the transmission ratio. In this case we also need to know the chord lengths l. The value of l is calculated based on the geometry of CT scanner and the dimension of the scanned object.

The first step is to decide on the pixel size or the dimensions of the elements of the matrix used for the discretization of the reconstruction domain. The circular section of the column is encompassed by a square, as shown in Figure 3.14. The size of the pixel depends on the achievable spatial resolution, or the width of the detector collimator. An even number of pixels is required on each side of the matrix, and given the achievable resolution, a suitable number of pixels are chosen. In this process, the linear attenuation coefficient in each pixel was verified for gas and solids phases. In the current study 100 pixels was chosen in the image reconstruction.

The special resolution is defined as,

$$d_{eff} = \frac{1}{M}\sqrt{d_a^2 + (M-1)^2 S^2} \quad \text{..... (37)}$$

where d_a is the detector collimator slit width, S is the source width and M is the magnification factor (equal 1 assuming source width is the same as the detector collimator width). In the current study, the slit width of 2 mm has been used and the special resolution can be specified as 2 mm. The corresponding size of the pixel is calculated given the diameter of the test section (typically the outer diameter of the column). In this reconstruction step, the angle subtended by the test section on the source (fan angle) need be identified (see Figure 3.13). Given all the needed parameters, this step computes, for all the projections in all the views, the identity of all the pixels through which the projection pass through, as well as the length of intersections of the beams with all those pixels. It also determines for any given pixel, the identity of all the rays that pass through it, as well as the length of intersection of each of those rays with that pixel.

e. Assigning initial guess values

Since the AM reconstruction algorithm is an iterative process, we need to provide the initial guess values for the attenuation coefficient in each pixel. The initial guess values are generated by assigning 0.08 (the linear attenuation coefficient of water, units cm^{-1}) to all the pixels in the square matrix which falls within or on the boundary of the test section, as shown in Figure 3.14. The choice of the magnitude is arbitrary and only affects the required number of iterations in the reconstruction process. For the pixels that are fully outside the test domain, 0 is assigned.

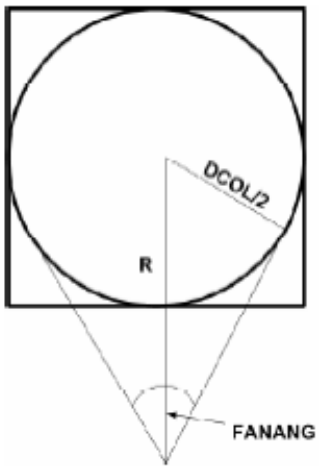

Figure 3.13: Geometrical features of a test section

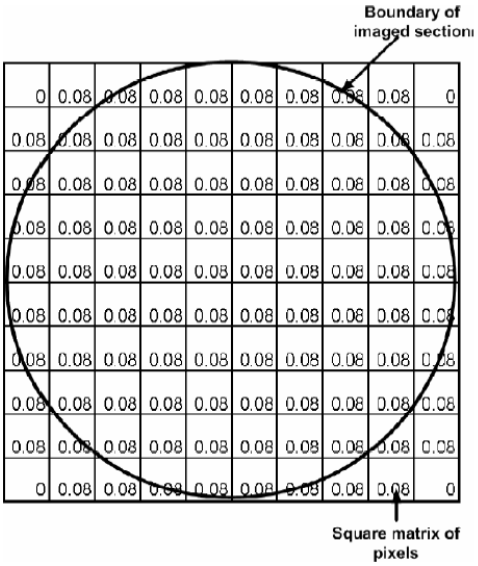

Figure 3.14: Discretization of domain cross-section

f. Image reconstruction

AM algorithm

In this step, the image reconstruction algorithm (AM) is used to obtain the attenuation coefficient values on the domain. The output file provides a matrix of the numbers corresponding to the linear attenuation coefficient in each pixel of the discretization chosen for the cross-section being reconstructed. The reconstruction algorithm is based on a statistical model for the measured data, Beer's law and a realistic model for the known point spread function [70]. The reconstruction problem is formulated as an optimization (maximum likelihood) problem in the statistical estimation theory. For more details, see Varma (2008) [22] and Varma et al. [72] & [73].

Calculation of Phase Holdup

The first step in obtaining holdup distribution profile is to obtain the attenuation image from the raw scanned data. The attenuation (μ) profile of any object is quantified by Equation (36) above. If the medium is made of two materials (such as solid and gas in this case) with mass attenuation coefficients μ_s for solid and μ_g for gas, densities ρ_s for solid and ρ_g for gas, and thickness l_s for solid and l_g for gas, then the total attenuation A is

$$A = \rho_s\mu_s l_s + \rho_g\mu_g l_g \quad \text{..... (38)}$$

Since $l_s = \varepsilon_s L$ and $l_g = \varepsilon_g L$, where $L = l_s + l_g$ then

$$A = [\rho_s\mu_s\varepsilon_s + \rho_g\mu_g\varepsilon_g]\, L \quad \text{..... (39)}$$

The summation of the holdups equals unity (i.e. $\varepsilon_g = 1 - \varepsilon_s$) then Eq. 38 become

$$A = [\rho_s\mu_s\varepsilon_s + \rho_g\mu_g(1-\varepsilon_s)]\, L \quad \text{..... (40)}$$

The measured quantity $ln\ (I/Io)$ is equal to the integral sum of the attenuation through the material along the beam path. For tomography, attenuations are measured along a number of such beam paths through the object from different directions around it. Given a set of attenuation measurements, the density distribution (image) can be reconstructed by using a suitable reconstruction algorithm. In the present study, an Alternating Minimization (AM) algorithm is being used to quantitatively determine the holdup distribution images of the packed bed with marbles.

Since the medium in the ij^{th} pixel is made of two materials, then the total line attenuation $A_{s\text{-}g,ij}$, can be written as

$$A_{s\text{-}g,ij} = [\rho_s\mu_s\varepsilon_{s,ij} + \rho_g\mu_g(1-\varepsilon_{s,ij})]\, L_{ij,} \quad \text{..... (41)}$$

where $\varepsilon_{s,ij}$ and $\varepsilon_{g,ij}$ are the holdups (volumetric fractions) of the solid and gas phases respectively, and $L_{ij,}$ is the length along which a particular gamma ray beam passes through the pixel.

Since $\rho_g << \rho_s$, the attenuation caused by the gas phase is negligible ($\mu_g \sim 0$), and L_{ij} is common for all A's in a single pixel. Hence, solids holdup in pixel ij can be written as follows

$$\varepsilon_{s,ij} = A_{s\text{-}g,ij} / \rho_s \mu_s, \quad \text{.....(42)}$$

The linear attenuation values obtained by using the reconstruction program for the packed solids can directly be used in place of $A_{s\text{-}g,ij}$. The mass attenuation coefficient of solids (μ_s) was calculated experimentally by using the CT scan setup as a gamma-ray densitometry device and applying the Beer Lambert's Law to measure the attenuation μ for one marble ball attached to the detector collimator. The μ can also be determined by using standard tables (such as NIST Physical Data) if the material composition of solids is precisely known. Finally, the void fraction distribution was determined using the expression

$$\varepsilon_{g,ij} = 1 - (A_{s\text{-}g,ij} / \rho_s \mu_s) \quad \text{.....(43)}$$

3.4 DSCT FACILITY

3.4.1 Description of Physical Components. The DSCT scanner at Missouri S&T uses the newer generation of double fan-beam scanning configuration. The configuration of the scanner consists of two arrays of NaI (Tl) detectors of 5 cm in diameter (15 detectors were used for each side) and two encapsulated sources ~ 230 mCi ^{137}Cs and ~ 22 mCi ^{60}Co. Both the point sources are housed in a shielded container, a part of which is opened when the gamma beam is required for the CT experiments. This device selectively collimates the beam to give it a fan shape. The two sources were designed and fabricated by at the Oakridge national laboratory (ORNL). Details of the source location in the shielded container, the operation protocol, the machines drawings giving details of the dimensions and some additional photographs related to them are available in Varma (2008) [22]. These sources are located opposite to the center of the each array of detectors, placed 120 cm apart. The total angle between the central axis of the 1st and the 15th detectors in the fan beam is 38.402° (see Figure 3.15). In this study,

only the ^{137}Cs source is used as we works with two phases in time. The detectors and the source are mounted on a plate which can be rotated 360º around the object using a stepper motor. Moreover, the whole assembly can be moved up and down along the column to scan different axial levels of the column. DSCT can scan columns up to 9 ft in height and 24 inches in diameter. The detectors are placed in an arc shape at 114 cm radius with the center of the source device. Each of these detectors is collimated with a lead collimator that is about 6.35 cm thick and has an open aperture of dimension 2 mm×5 mm. This aperture reduces the effective exposed area of the crystal to a rectangular region of dimension 2 mm×5 mm. The counts received by the detectors are limited to what is incident on this aperture. This detector array is moved with a stepper motor 21 times at an angle of 0.13° from the source, thereby creating 315 detector positions effectively for each source position. The projection is modeled as a fine line between the source and the detector as the open area of the detectors is very small. A total of 197 views or source positions are considered; hence, gamma ray counts data for 315×197 (total 62055) projections passing through the domain are collected. The un-attenuated gamma ray photon counts of 662 keV were recorded. A 100×100 pixels resolution is used to reconstruct the image. Hence, each pixel represents an area of 2 mm×2 mm of the object.

3.4.2 Electronic Hardware and the Data Acquisition System. The data acquisition system is consists of the detectors, preamplifier, pulse processors and stepper motors that automate the motions involved in the CT system. The solid state scintillation detectors (made by Bicron) were used in the experiments. Each detector assembly consisting of a 2”×2” NaI(Tl) crystal in an aluminum housing, a photomultiplier tube directly mounted to crystal housing, an internal magnetic/light shield followed by preamplifier (see Figure 3.16). A 2”×2” crystal has about 70% absorption efficiency for ^{137}Cs source and the best resolution achievable ranges from 7.5%-8.5% for 662 KeV gamma ray [74].

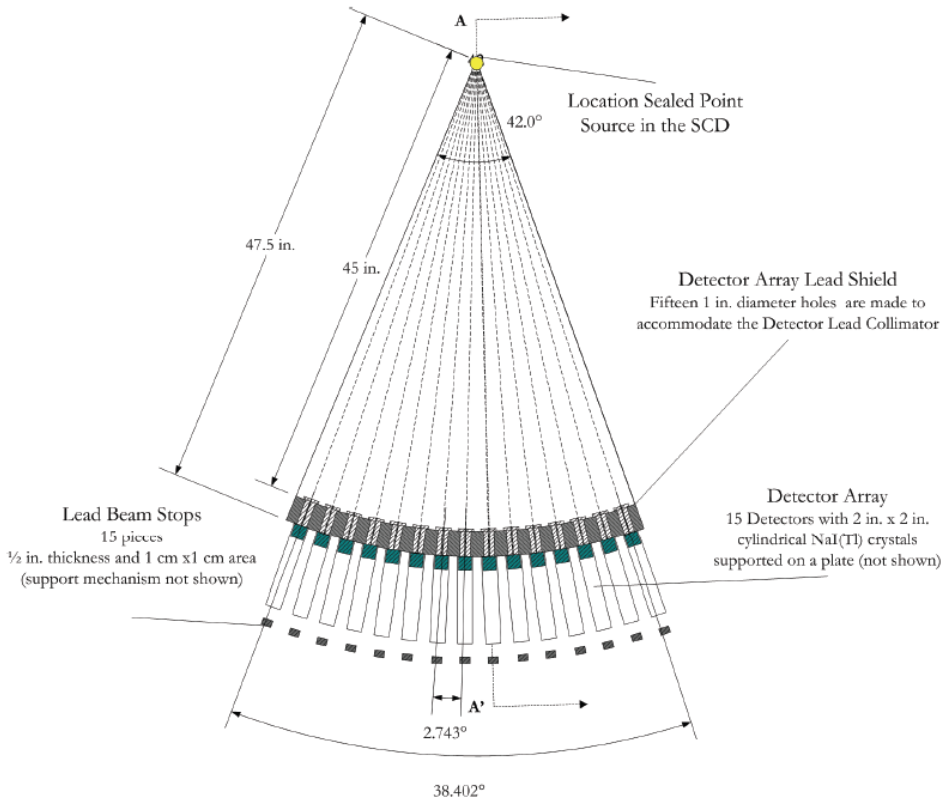

Figure 3.15: Schematic (top view) showing the fan beam arrangement of the source-detectors with the detectors collimators [taken from 22]

The Canberra preamplifier Model 2007 was used. The preamplifier is connected directly to the photomultiplier tube (PMT) containing a high voltage divider network to supply voltage for the PMT and the Anode output signal. The detectors are powered by a Canberra power supply. The signal from the preamplifier, attached to the detector, is fed to the timing amplifier. This is in turn passed on the multilevel discriminator and a scalar. The final data is stored in the computer in form of a data file. A photograph of the timing amplifier and the crate controller computer are shown in Figure 3.17. The electronic modules associated with the NIM bin crate and the PCI crate was developed at the Oakridge National Laboratory (ORNL). A C++ based program called *Biomass.c* developed by (ORNL) was used to perform the CT scan and to acquiring the data. Details

of the data acquisition modules and the operation of *Biomass.c* have been discussed elsewhere [75].

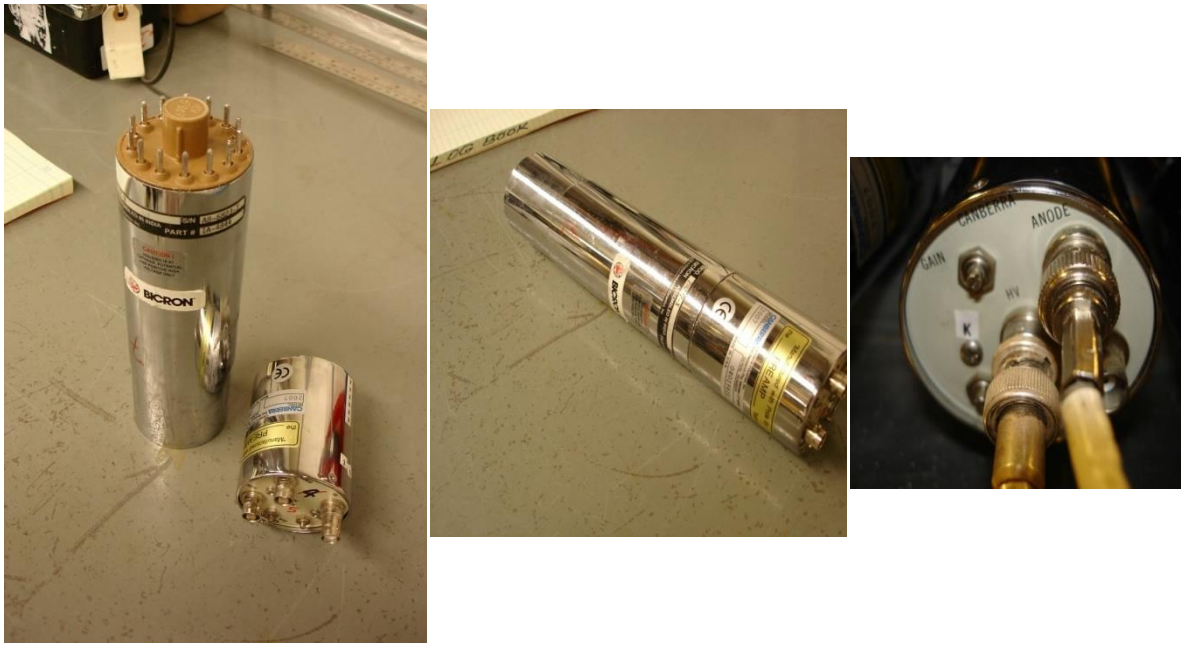

Figure 3.16: The NaI(Tl) solid state scintillation detector assembly

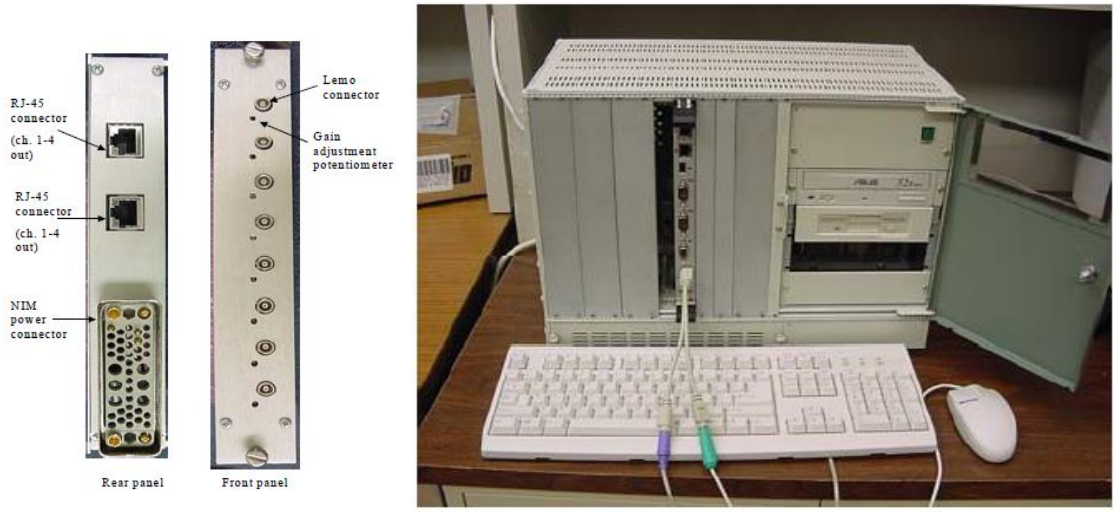

Figure 3.17: Shaping amplifier module (left) and the crate controller and single board computer (right)

Figure 3.18 shows the schematic diagram of the DSCT data acquisition system. Many useful parameters such as sampling frequency, acquisition time, number of sampling and others can be specified in an input text file fed to *Biomass.c*. The source-detector alignment (centering) was made by using a highly directed laser beams. The laser devices were placed in an aluminum housing that has the same dimensions as the NaI detector and can easily replace any detector position.

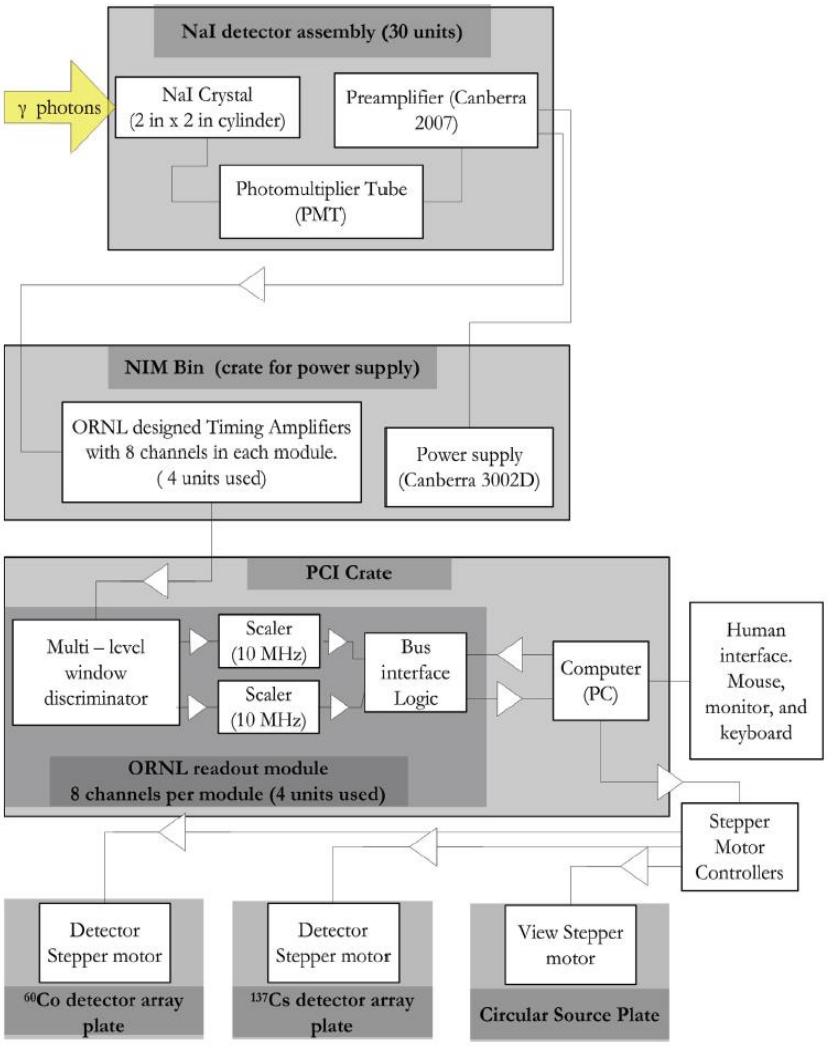

Figure 3.18: Schematic diagram of the data acquisition system used in the DSCT system

3.5 CT-SCAN SYSTEM VALIDATION

Before implementing the Computed Tomography (CT) technique for the structural characterization of pebble bed, a set of phantom based experiments were carried out to validate the CT measurements, programs and image reconstruction algorithms used with DSCT modality. The test phantom (Figure 3.19) used in this study is made of Perspex. The phantom represents a circular domain of 15.24 cm (6 inch) diameter consisting of two sections; the inner section has 7.62 cm (3 inch) inside diameter whereas an outer annulus section has diameter of 15.24 cm (6 inches). Different cases such as air is in the inner section and water is in the outer annular section (case I), air is in the outer annular section and water is in the inner section (case II) and water is filled in both the outer and inner sections (case III) were tested for validation of CT based experiments

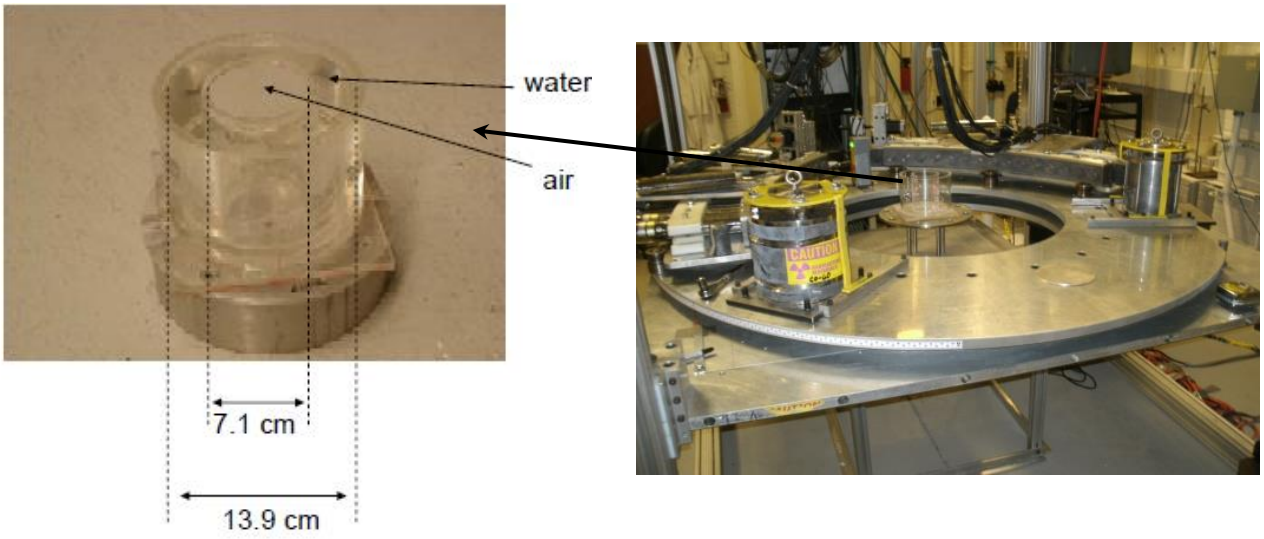

Figure 3.19: Picture of the 6" phantom (Perspex) used in the CT scan experiments with two phases (case 1**)**

In each experiment the attenuation images were obtained by determining the background scans where the domain purely consists of only one phase (such as air gas) and another scan for the two phases (liquid-air). The averaged data from the CT scan files for water-air phases, along with the data file for air only were used to calculate the transmission ratio (I/I_0) of the scanned phantom. Figure 3.20(A) shows a typical transmission ratio plot for the 6 inch phantom (case 1). The plot illustrates smooth and symmetric along the center. It is always suitable to make such a plot as an intermediate step in the reconstruction process to assess the correctness and quality of the scan. The Sinogram tool has been implemented in this study to visualize the attenuation values for all positions of source and detectors. Sinogram image shown in Figure 3.20(B) for the case 1 was reconstructed using the transmission calculated from the measured counts. Each pixel in the Sinogram represents the transmission ratio for the corresponding projection number given. Figures 3.21 and 3.22 show the transmission ratio and Sinogram for the cases 2 and 3, respectively. The alternating minimization (AM) algorithm [71] was employed to process the CT scanner data and to reconstruct and validate the phantom data.

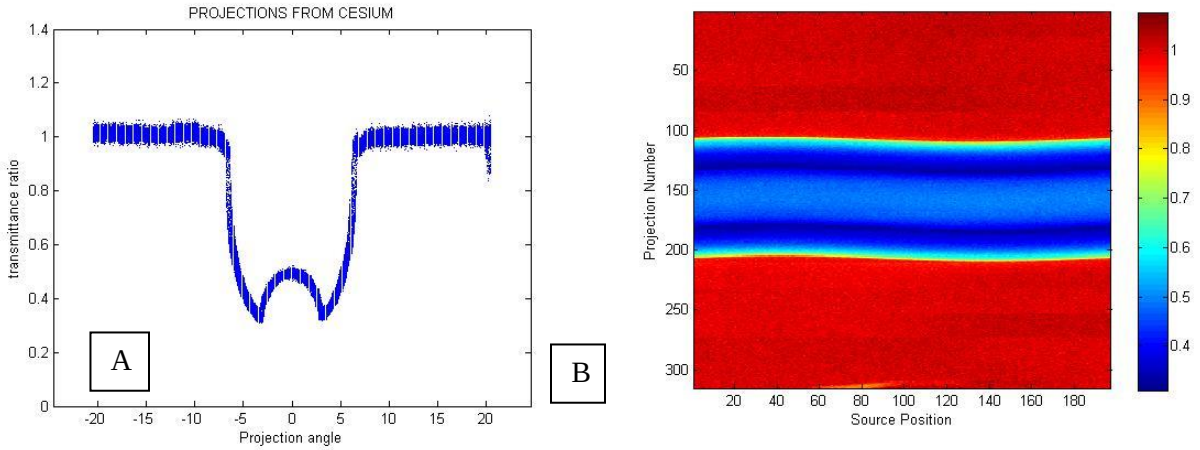

Figure 3.20: (A) the transmission ratio (I/I_0) for the phantom (case 1) (B) The Sinogram of the phantom attenuation coefficients for case 1

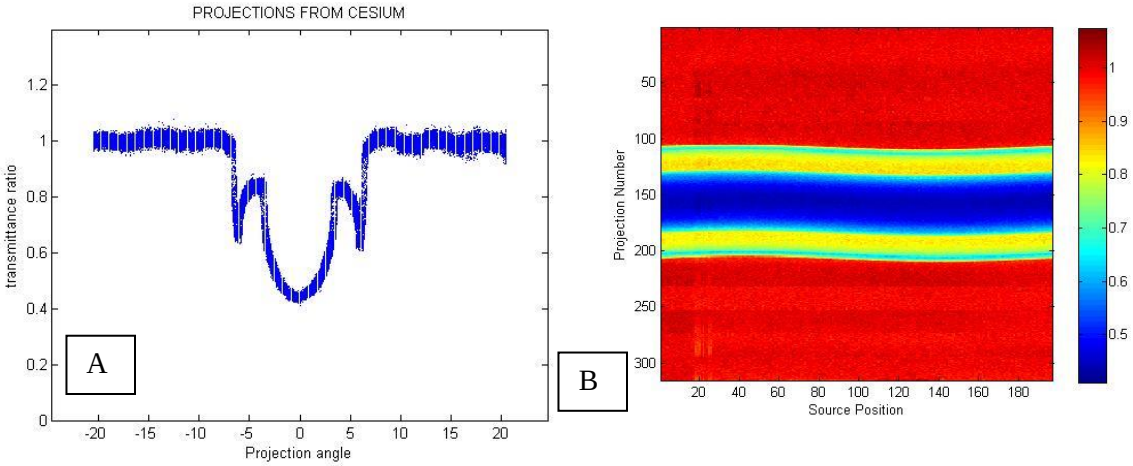

Figure 3.21: (A) the transmission ratio (I/I_0) for the phantom (case 2) (B) the Sinogram of the phantom attenuation coefficients for case 2

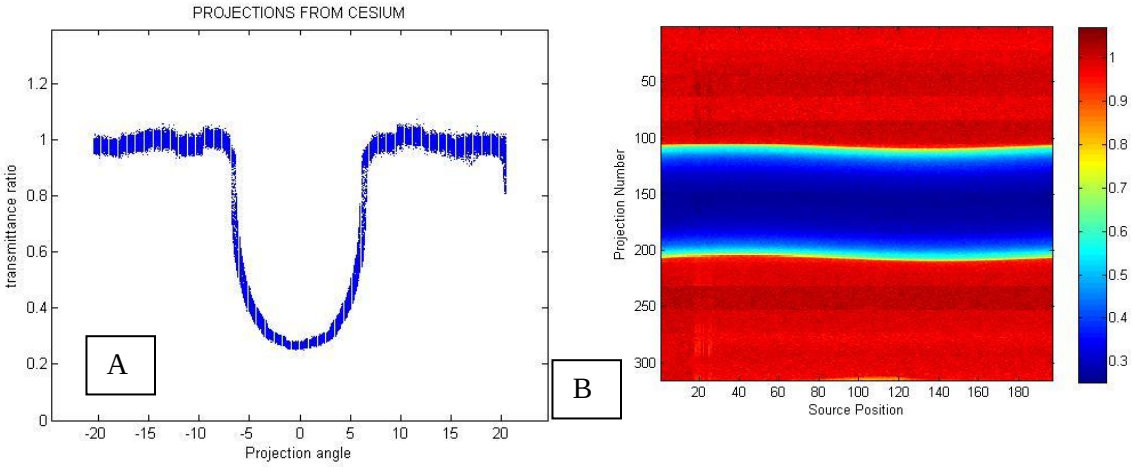

Figure 3.22: (A) the transmission ratio (I/I_0) for the phantom (case 3) (B) the Sinogram of the phantom attenuation coefficients for case 3

The mean attenuation values obtained from AM algorithm showed that the attenuation image of the scanned domain matched closely the theoretical values for water and air linear attenuation coefficients of 0.0857 and 0.001 cm^{-1} respectively.

Also, the obtained dimensions of the phases by CT are close to the phantom's dimensions with discrepancy of 0.84% (see Figure 3.23).

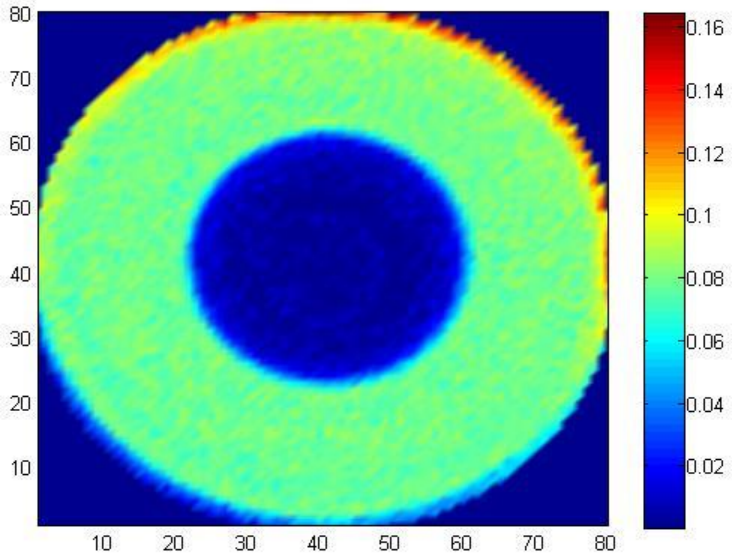

Figure 3.23: The linear attenuation coefficient distribution for the two phase phantom (AM image reconstruction**)**

4. RESULTS AND DISCUSSION

All experiments were conducted in a 1 foot diameter column that was packed randomly with glass spheres of different sizes (0.5, 1 and 2 inch). The gamma ray scanner was comprised of a collimated ^{137}Cs gamma source, an arc of 15 radiation detectors, and a data acquisition system. Each of these detectors was collimated with a lead block that housed the detector with an open aperture of 2 mm to eliminate any scattered gamma photons from counting in the detectors. The source and the detectors were mounted opposite to each other on a circular scanner plate. This plate could be rotated 360^{o} around the pebble bed. The entire assembly could be moved up and down along the test section so that different axial levels could be scanned. The gamma-ray CT system used is pictured in Figure 4.1. This system contained one foot pebble bed reactor that was filled with 0.5 inch glass spheres.

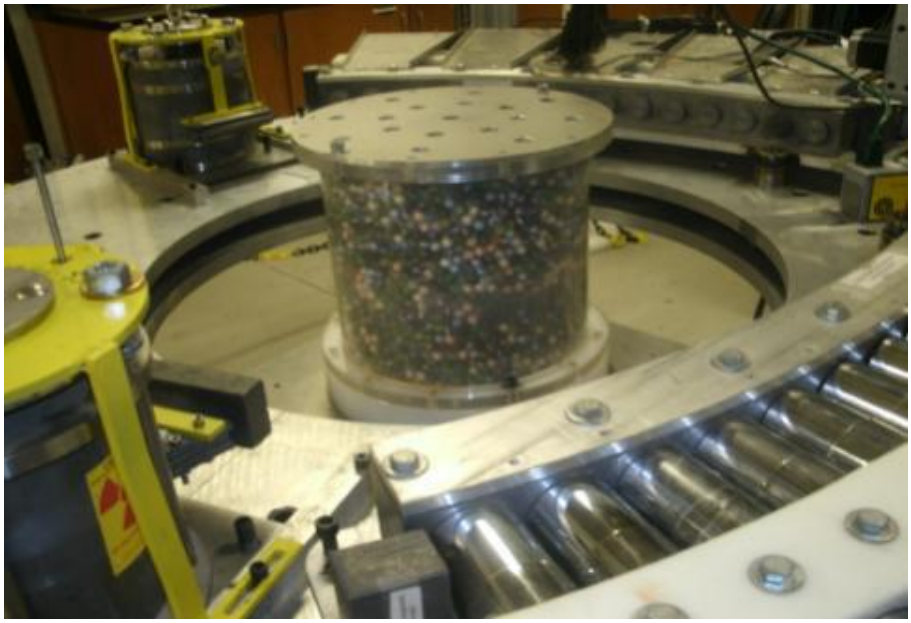

Figure 4.1: Experimental setup of a 1 ft diameter pebble bed packed with 0.5 inch glass spheres inside the CT scanner

The main focus of this work is to quantify the void and solids holdup distribution across the two dimensional domain in randomly packed pebble beds. Several, CT scans were performed in specific conditions so that sufficient data for holdup calculations (e.g., scan with air only between the source and the detector and scan for the packed bed) could be collected. The algebraic algorithm of Alternating Minimization (AM) was applied to determine the attenuation coefficient values (μ) on the domain. The linear attenuation coefficient in each pixel was verified for gas and solids phases. One hundred pixels were chosen in the image reconstruction process; the special resolution for these experiments was 2 mm.

In the subsequent sections the measurements of the void fraction and solids distribution in a pebble bed reactor were presented. The radial distribution profiles of the void fraction within the pebble bed were also obtained along with the void probability distribution.

4.1 VOID FRACTION DISTRIBUTION IN PEBBLE BED REACTOR

The void fraction distribution in pixel *ij* was determined using Equation (43) above,

$$\varepsilon_{g,ij} = 1 - (A_{s\text{-}g,ij} / \rho_s \mu_s)$$

where $A_{s\text{-}g,ij}$ is the total line attenuation for the gas and the solid in the ij^{th} pixel, and ρ_s and μ_s are the solid's density and mass attenuation coefficient, respectively. The mass attenuation coefficient can either be calculated experimentally or determined with standard tables (such as NIST Physical Data). As mentioned before, the linear attenuation values obtained through the reconstruction program for the packed solids can be used in place of $A_{s\text{-}g,ij}$. The time averaged cross-sectional solids and voids profiles can be represented in two ways. A color contour plot is used as part of the first method to plot the cross-sectional distribution of different phases. The second method is based on the circumferentially averaged the pixels of the cross sectional distribution. The following equation is then applied so that the result can be plotted as averaged radial variation of the void fraction:

$$\bar{\varepsilon} = \frac{2}{R^2}\int_0^R \varepsilon(r) r dr \quad \text{..... (44)}$$

A cross-sectional void fraction distribution of a pebble bed packed with 1 inch pebbles is given in Figure 4.2 at three axial levels (3, 6, and 9 inches above the bed base). The details illustrated in these images are important to understanding the structure of a packed sphere: different planes have different void distributions. These distributions are dependent on the internal friction between the spheres and between the spheres and the column wall. The planes (cross-sections) are separated by nearly 3 inches (3 sphere diameter).

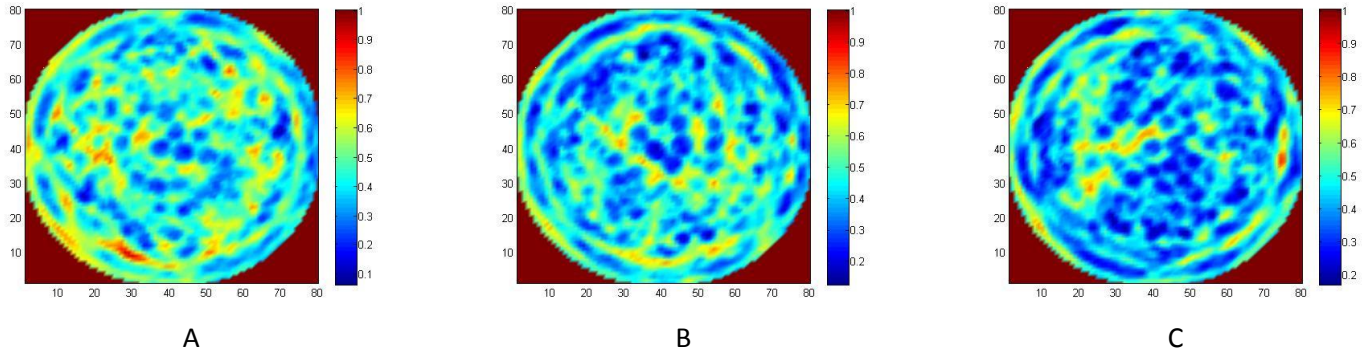

A B C

Figure 4.2: Time averaged cross-sectional void fraction distribution in a 12 inch packed bed column that was filled with (1 inch) marbles at (A) 3 inches, (B) 6 inches, and (C) 9 inches, from the base of the bed

Figure 4.3 shows the cross-sectional void fraction distribution of a pebble bed at different pebble sizes (0.5 inches, 1 inch, and 2 inches, respectively) at the bulk region (bed center). As shown in this figure, the gamma ray tomography technique provided a clear graphical representation of the different phase distributions that occurred in cross-sections of the packed pebble bed column. The pixels with red level values are directly related to the highest void fraction at that specific condition. Several pockets (blue areas) of high porosity zones occurred within the pebble bed's distribution. Histograms were used to further analyze the void distribution images (see Appendix A, outlines the computer program). These histograms were generated from the experimental data gathered; they were used to quantify the void variations. The probability distribution

conformed to a normal distribution pattern in all three of the packing sizes. The void distribution was strongly depends on the pebble size or the aspect ratio ($D_{column}/d_{particle}$).When the pebble's diameters increased from1.27 cm (0.5 inch, D/d=24) to 2.5 cm (1 inch, D/d=12), the variance of void increased by 2.3%. The void's spreading increased by 198% when the pebble's diameter increased from 2.5 cm (1 inch) to 5 cm (2 inches, D/d=6). The void fraction was relatively higher near the wall and lower in the center.

4.2 AVERAGED RADIAL PROFILES OF THE VOID DISTRIBUTION

The radial void variation is another characteristic structural feature of confined fixed packed beds. It is produced by the influence of column walls [56]. Both axial and radial porosity (void) variations present have a strong influence on the fluid's flow. Hence, they also influence the heat and mass transfer present in the fixed-bed reactors. The radial void distribution profiles for the three different pebble diameters at different axial levels of the pebble bed are given in Figure 4.4. The oscillations are quite large near the wall, with a minimum void fraction of 0.33 at a 0.68 d (0.68 pebble diameter) from the wall (for 2 inch pebble size). One would expect the void fraction would to go to unity near the wall**,** since the solids have point contacts at the walls. However, a slight drop occurred (0.85). This drop was caused by the gamma attenuation that occurred within the column wall itself. Also, the pixel used for calculations at the wall would lower the void fraction measurements. In general, the gamma sampling volume observed was too large to clearly reveal any trends that may have occurred within one particle size of the wall and to capture the point contacts of the particles with the wall [17 and 40]. Several pockets of voids occurred near the center of the pebble bed as a result of the random packing process. Thus, the trend, at times, exhibited a slight rise in the void fraction. Due to large local void volume obtained with relatively large size pebbles (> 2.5 cm) and the structural inhomogeneities of such randomly packed pebbles, different heights of CT scans give varying trends of the radial porosity profiles and its oscillation. The radial void fraction profiles had similar oscillating trends from the wall as compared to the recent literatures for the cylindrical packed systems with different ratios of column diameter to sphere diameter [23, 34, and 76].

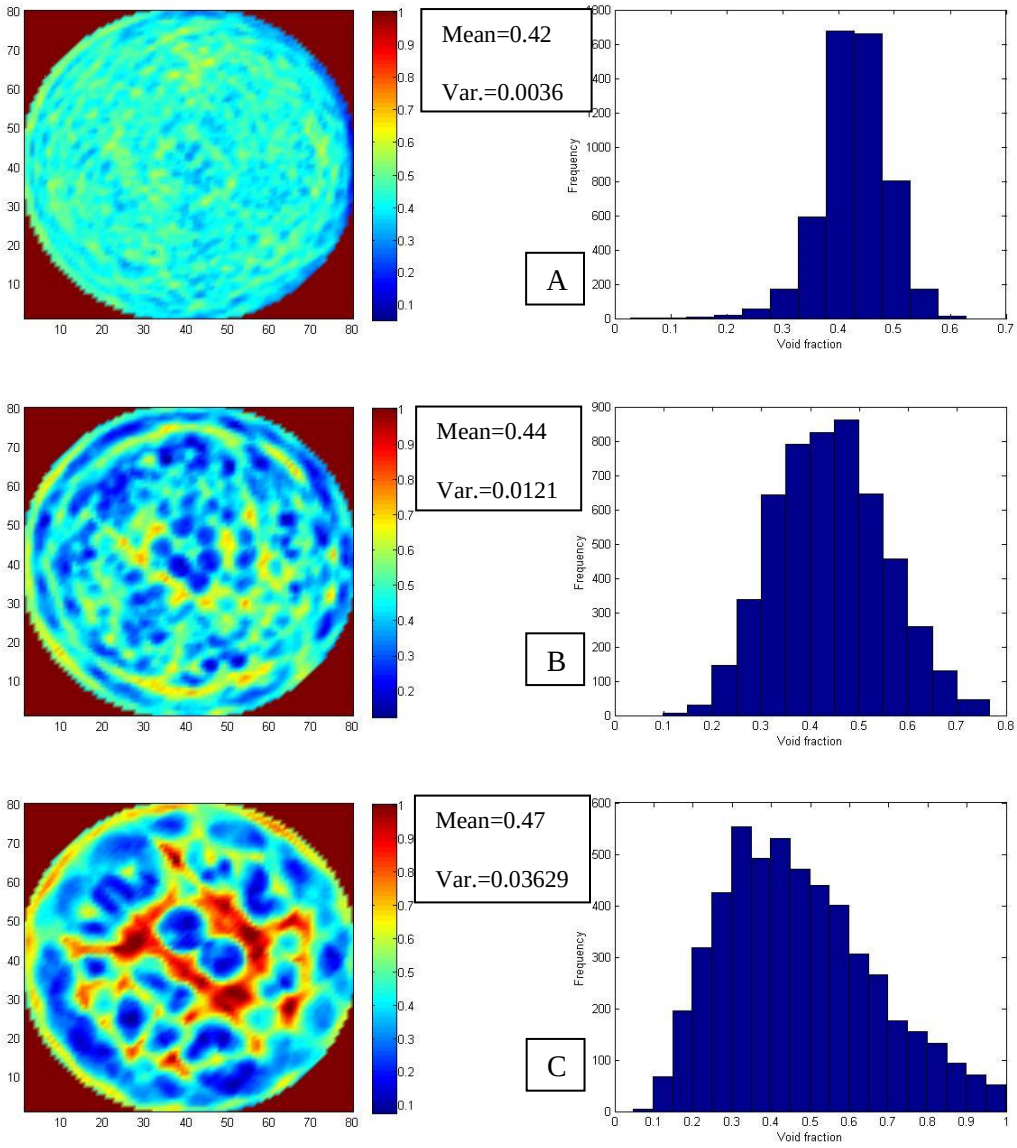

Figure 4.3: Time averaged cross-sectional void fraction distributions (in the left column) and histograms of local void distributions at the pebble bed's middle section (6 inch from the base) (in the right column) with pebble sizes of (a) 1.27 cm, (b) 2.54 cm, and (c) 5 cm.

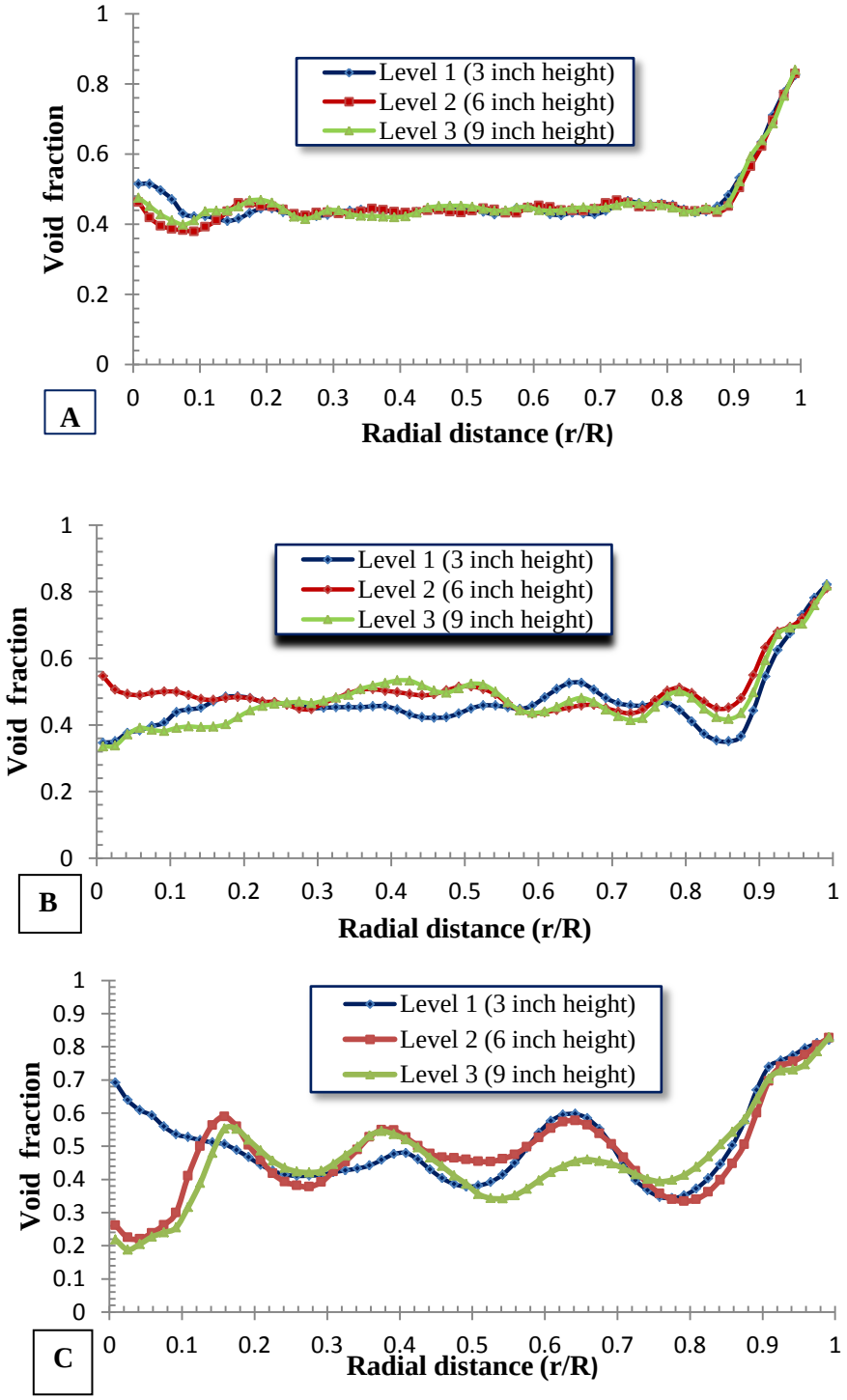

Figure 4.4: Radial void fraction profiles for the three different pebble diameters (d_1=1.27 cm, D/d=24), (d_2=2.54 cm, D/d=12) and (d_3=5 cm, D/d=6) at different levels L_1=7.62 cm (3 inch)**,** L_2=15.24 cm (6 inch) and L_3=22.86 cm (9 inch)

4.3 EFFECTS OF VARIOUS PARAMETERS ON VOID DISTRIBUTION

Effects of pebble size, packing reproducibility and bed height on the void distribution have been studied and discussed below.

a) Effects of pebbles size on void distribution

The azimuthally time averaged radial void profiles for the three pebble diameters (1.27 cm, 2.54 cm and 5 cm), at the bulk region of the pebble bed are depicted in Figure 4.5. The radial profile for the 5 cm pebble oscillated strongly from the wall toward the bed's center because these sizes of pebbles provided larger local void volumes. Smaller pebble sizes (1.27 cm) oscillated less than did the other two bigger diameters. The smaller pebble's radial void fraction profile, with a minimum void fraction of 0.43, was almost 4 pebble diameters away from the wall; while it was 0.37 at less than 1 pebble diameter with a 1 inch pebble size and 0.33 at a half pebble diameter with a lager pebble size (2 inch). The void fraction fluctuated around the mean, with a lower value (0.27), near the center of the packed bed and a higher value at the wall region (0.85); see Figure 4.5.

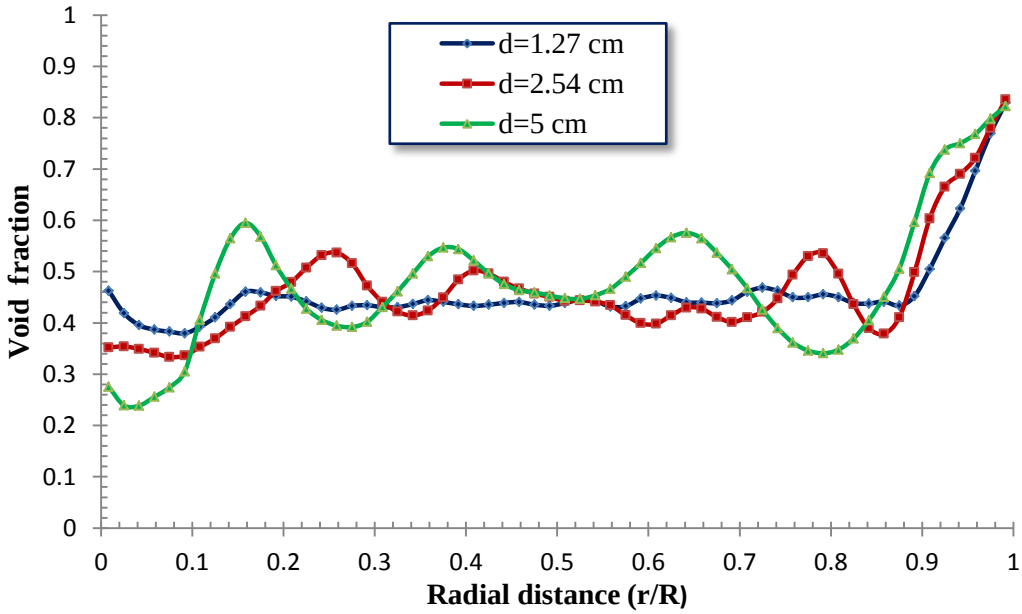

Figure 4.5: Radial void fraction profiles for the three different pebble diameters (d = 1.27 cm, 2.54 cm and 5 cm) at the bulk region level (bed center or 6 inch from the base)

b) Reproducibility of the packing method

The pebble bed reactor analyzed in this experiment consisted of a 1 foot high Plexiglas column that was packed with 1 inch glass spheres (pebbles). The pebbles were poured gently (loosely) into the bed container. Three CT scans were performed at three axial levels (3 inch, 6 inch, and 9 inch from the bottom of the column). At end of this experiment, the pebbles were discharge from the bed and put in an external vessel then the pebbles were reloaded again into the column in the same packing way (gently pouring the pebbles into the container without any pressure or vibration) to check for reproducibility. Three CT scans were performed at the same axial levels used during the first packing mode. A comparison between the radial variations in the void distribution of the two packing at the three different levels is given in Figure 4.6. The effect of repeating the bed packing (packed 1 and packed 2) was significant on the void distribution away from the wall due to the stochastic nature of random packing used. The figure also shows that the variation in radial void distribution for both packing is still in a good agreement near the wall region. The average value of discrepancy for the both trends at the bulk region (Figure 4.6-B) was 13% and it is 1% at the wall region and 48% near the center.

c) Effect of bed height on void distribution

An additional 1 foot tall column was added to the top of the original column. This additional column was filled with 458 pebbles (each 2 inches in diameter). Irregular pebbles were removed to keep upper surface as flat and uniform as possible. The radial void fractions of the three levels (3 inches, 6 inches, and 9 inches above the base) within the bed that was one foot for bed (packed with 226 pebbles) and two feet tall (packed with 458 pebbles) are plotted in Figure 4.7. These profiles had the same oscillatory behavior in the void's variation in the radial direction, at all three levels. Adding an additional packed section did not affect the radial void distribution in the first pebble bed section (lower column). These results are in agreement with Toit's [29] finding; a pebble bed reactor's packing seems to be a slightly looser packing, and the sphere's weight does not seem to have a significant impact on the void bulk value's uniformity.

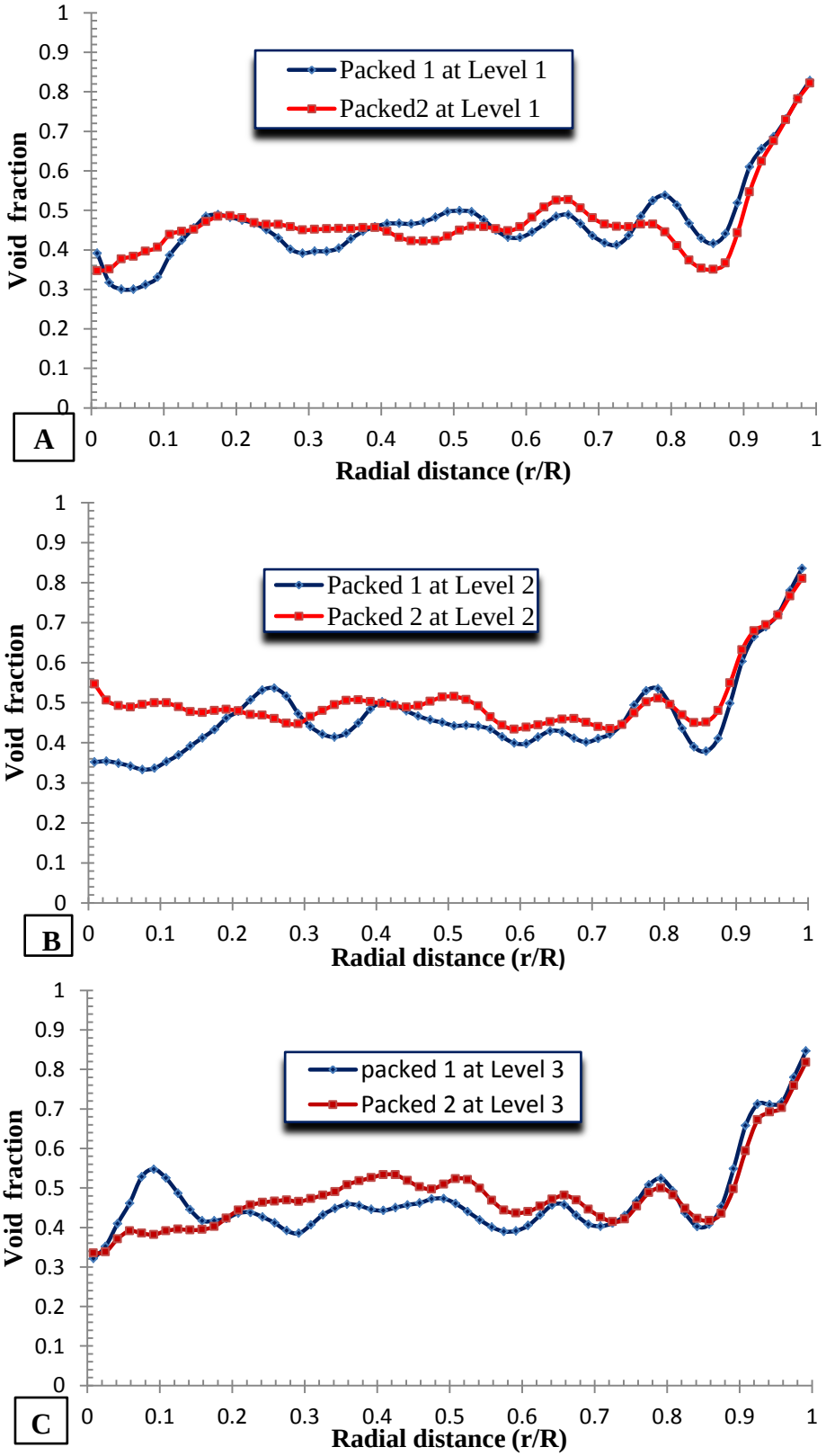

Figure 4.6: Radial void fraction profiles for the two packing reproducibility of one inch pebble at different levels (A: L1= 3 inch, B: L2= 6 inch and C: L3= 9 inch)

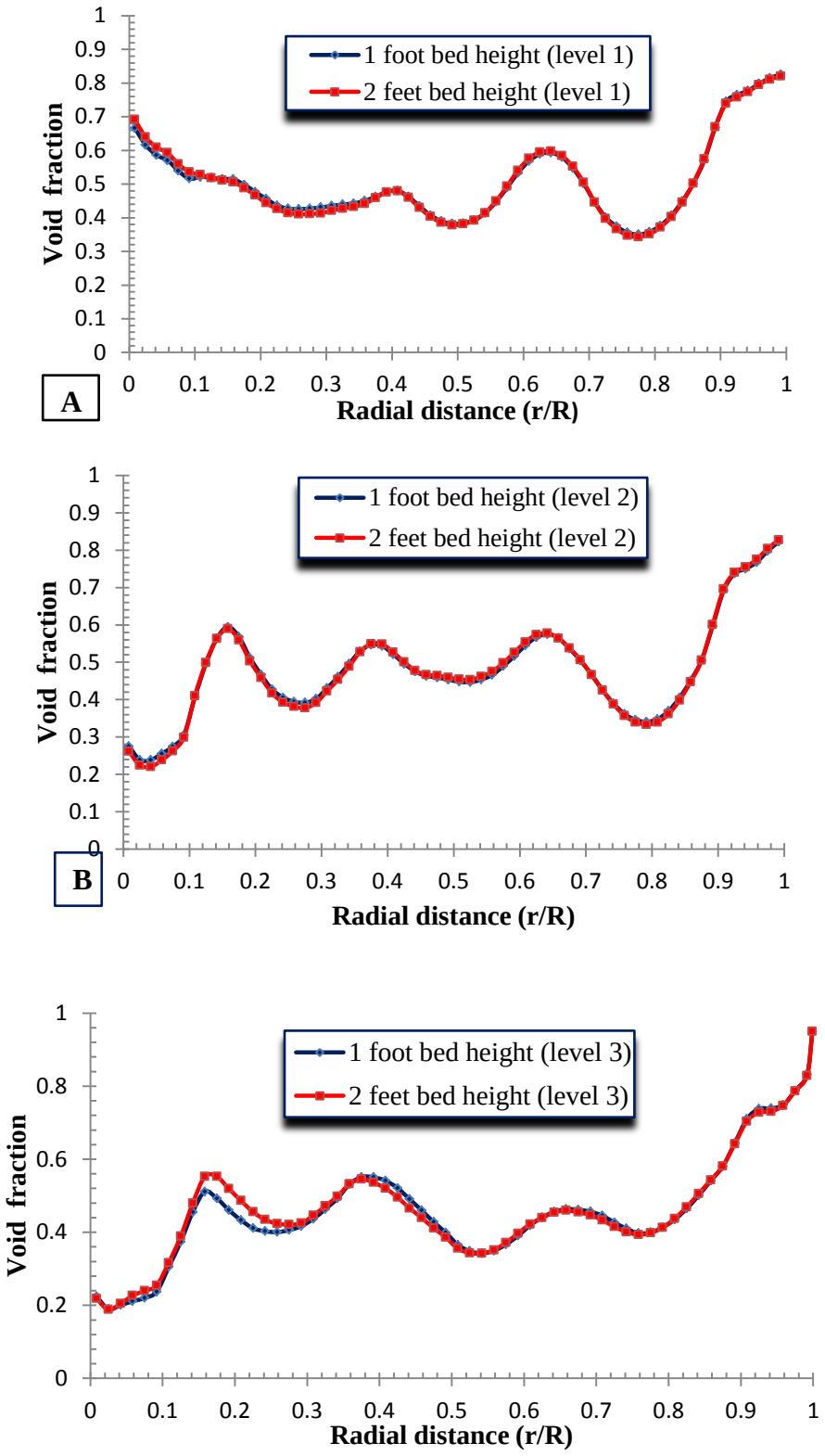

Figure 4.7: Radial variation in the void fractions of two bed heights at three different axial levels: A) 7.62 cm, B) 15.24 cm, and C) 22.86 cm)

4.4 AXIAL VOID FRACTION PROFILE AND 3D VISUALIZATION OF A PEBBLE BED REACTOR'S INNER STRUCTURE

The pebble bed reactor is a type of nuclear reactor design that contains approximately half a million fuel pebbles that form a heat-producing column. Knowledge of the packing's characteristics and the fuel pebble's behavior is important to accurately resolving core neutronics, burnup, and thermal-hydraulics.

A 3D visualization computer code must be used to predict the pebble bed reactor's packing pattern. Gamma ray computed tomography (CT) can be used to characterize materials in an effective, quantitative way.

A Plexiglas cylinder (one foot in diameter and one foot long) was used in this study. This cylinder filled randomly with 1750 glass spheres that were 1 inch in diameter. This setup was representing the core of a pebble bed reactor.

4.4.1 Axial Void Fraction Distribution in a Pebble Bed Reactor. Multi cross-sectional scans are needed to better understand the bed structure and its impact on a reactor's physics. Thus, 20 cross-sectional slices were scanned along the bed's height. The axial void distribution was used to estimate the bottom wall's influence on bulk organization. This distribution was obtained by counting the void fraction on each slice (azimuthally averaged) in the vertical direction which gives 20 data points (Figure 4.8). The fluctuation of the void fraction profiles (Figure 4.8) was plotted from the bottom to the top. The oscillations in the bed's bottom were more pronounced than those at the top because the spheres were more structurally packed in the bottom. No boundary effects in the axial profile's top region. This finding was expected because the upper side was a free boundary, which impressed no restraints on the pebble locations.

4.4.2 3D Visualization of the Pebble Bed Structure. A more detailed characterization of the bed structure is required to improve the knowledge of the mass and heat transfer models. This would also help to describe the interaction between pebbles and walls. Data obtained from several cross-sectional slices along the bed's height were used to develop a 3D visualization computer code. Twenty cross-section slices were used to reconstruct 3D images in a cylindrical column that was 1 foot tall and had a 1 foot inner diameter**.**

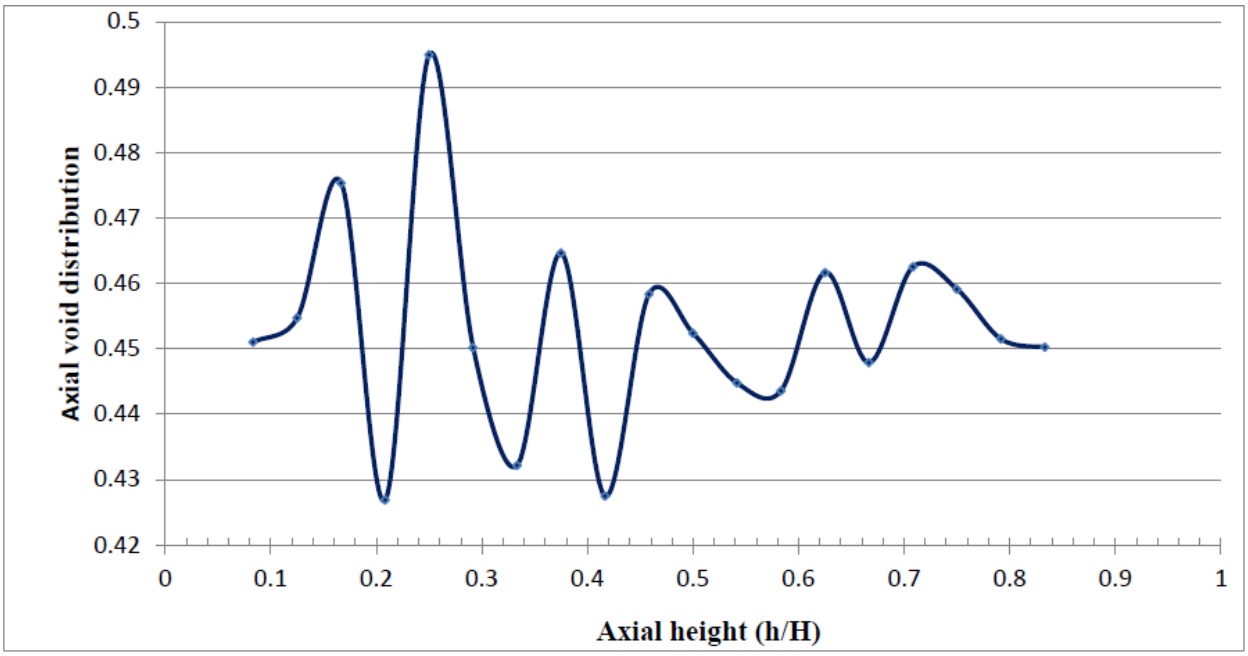

Figure 4.8: Axial void fraction distribution for (D/d=12) pebble bed reactor

This cylinder was packed randomly with 1750 1 inch glass spheres. Despite of the difficulties to visualize complex volume such as the pebble bed structure, attempt was made to reconstruct the 20 sectional slices, using gamma tomography, to obtain a 3D image of the entire bed with quantitative information about axial and radial void fraction distribution and is shown in Figure 4.9. With higher resolution data one can get even better illustration of the packing structure through the 3D visualization. The 2D reconstructed void data was concatenated along a specified 3D model. The data was then smoothed. A convolution operation was to filter the image linearly. Convolution is a neighborhood operation in which each output pixel is the weighted sum of the neighboring input pixels. The matrix of weights is referred to as the convolution kernel (also known as the filter). The isosurface data was computed last to create a 3D image. An isosurface is the 3D analog in an isoline; it is a surface that represents points of a constant value (e.g., void fraction) within a volume of space. Thus, an isosurface is a level set of a continuous function with a 3D-space domain. Isocaps were used to provide

a visual context for the isosurfaces. They offer a cross-sectional view of the isosurface's interior for which the isocap provides an end cap.

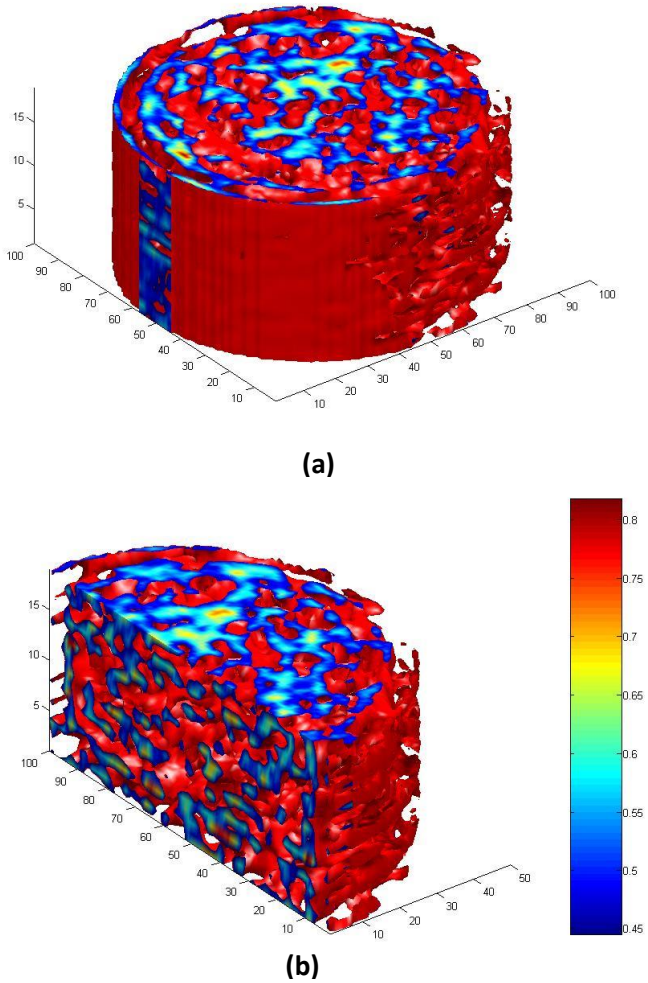

Figure 4.9: A visualization of the packing structure inside the cylindrical pebble bed showing the axial and radial void distribution (a) 3D view of the analyzed bed (b) Vertical cut section in the center of the bed

4.5 COMPARISON OF THE EXPERIMENTAL AND CALCULATED VOID FRACTION DISTRIBUTION

Randomly packed beds will exhibit non-uniform pebble densities, particularly near the wall. This non-uniformity will significantly affect the core neutronic and the thermodynamics due to wall channeling. Computational tools that can generate the pebble bed structure, as well as experimental data that can benchmark these tools, are needed to facilitate this research.

4.5.1 Average Void Fraction. The average void fractions used for both the experimental and the calculated methods are listed in Table 2. The average void fraction for the three aspect ratios used in this study can be found within this data. As expected, the average void fraction (porosity) of the bed increase as the ratio D/d_p decreased.

Table 4.1: Average bed void fraction obtained through either experimental or calculated methods

Aspect Ratio D/d_p	**Experiment**	**Jeschar**	**Dixon**	**de Klerk**	**Pushnov**	**Zou & Yu**	**Mueller**
24	0.413	0.389	0.403	0.41	0.377	0.374	0.374
12	0.426	0.403	0.407	0.413	0.382	0.377	0.383
6	0.472	0.432	0.42	0.444	0.403	0.396	0.402

The experimental data of the average void fraction was obtained from the circumferentially averaged void and solids in the reconstruction process. The averaged void fractions were averaged again for several cross-sections along the bed's height. The average void fraction introduced by various mathematical models indicates different values. This variance is attributed to the packing mode used and the particle's roughness. These two factors may influence the prediction of porosity in the bulk region (ε_b) [45].

4.5.2 Radial Void Fraction Profiles: A comparison between Experimental and Exponential Correlations. The variation in void fraction distribution in a fixed bed was modeled mainly with exponential expressions [17; 29; 35; 54]. A correlation proposed by Vortmeyer and Shuster (1983) [54] (which is widely used in the literature) was used here to predict the trends in void fraction's radial variations. It was assumed that the average porosity decays exponentially, from unity, at the wall to the bulk value, near the center. It is given by

$$\varepsilon_r = 1 - (1 - \varepsilon_b)\left\{1 - e^{-2\left(\frac{R-r}{d_p}\right)^2}\right\} \quad \text{(45)}$$

where ε_r is the void fraction in radial position r, ε_b is the void in the bulk region of the pebble bed, R is the radius of the packed bed column, and d_p is the pebble's particle diameter. The aim is to develop a better understanding of the variation in the void fraction (porosity) of annular pebble bed reactor by trying to quantitatively compare measured and calculated radial distribution of void fraction. This can help to make analysis and design of pebble bed reactors. The comparison between the exponential correlations for the radial variation in the void fraction (Eq. 45) and the CT experimental results is illustrated in Figure 4.10. Three different aspect ratios were identified in Figure 4.10. It is clear that the model did not describe the oscillatory nature and damping of the void variation near the wall as it is shown in terms of an exponential type function only. Agreement between the experimental results and the exponential expression model is better at a smaller sphere diameter (higher D/d_p ratio of 24) than it is at a larger sphere diameter. The more noticeable differences in Figure 4.10 can be observed in B and C as pebble diameter increases (D/d decreased). The average differences in Fig. 4-10-A is about 9.5% in the wall region and decreases to 1.2% away from the wall (about 6 pebble diameters). The oscillatory behavior in the void's variation, in the radial direction, was more significant when larger bed spheres were used. The overall average discrepancy between the experimental and the exponential correlation for Fig. 4.10-B is 13% and for Fig. 4.10-C is 21%.

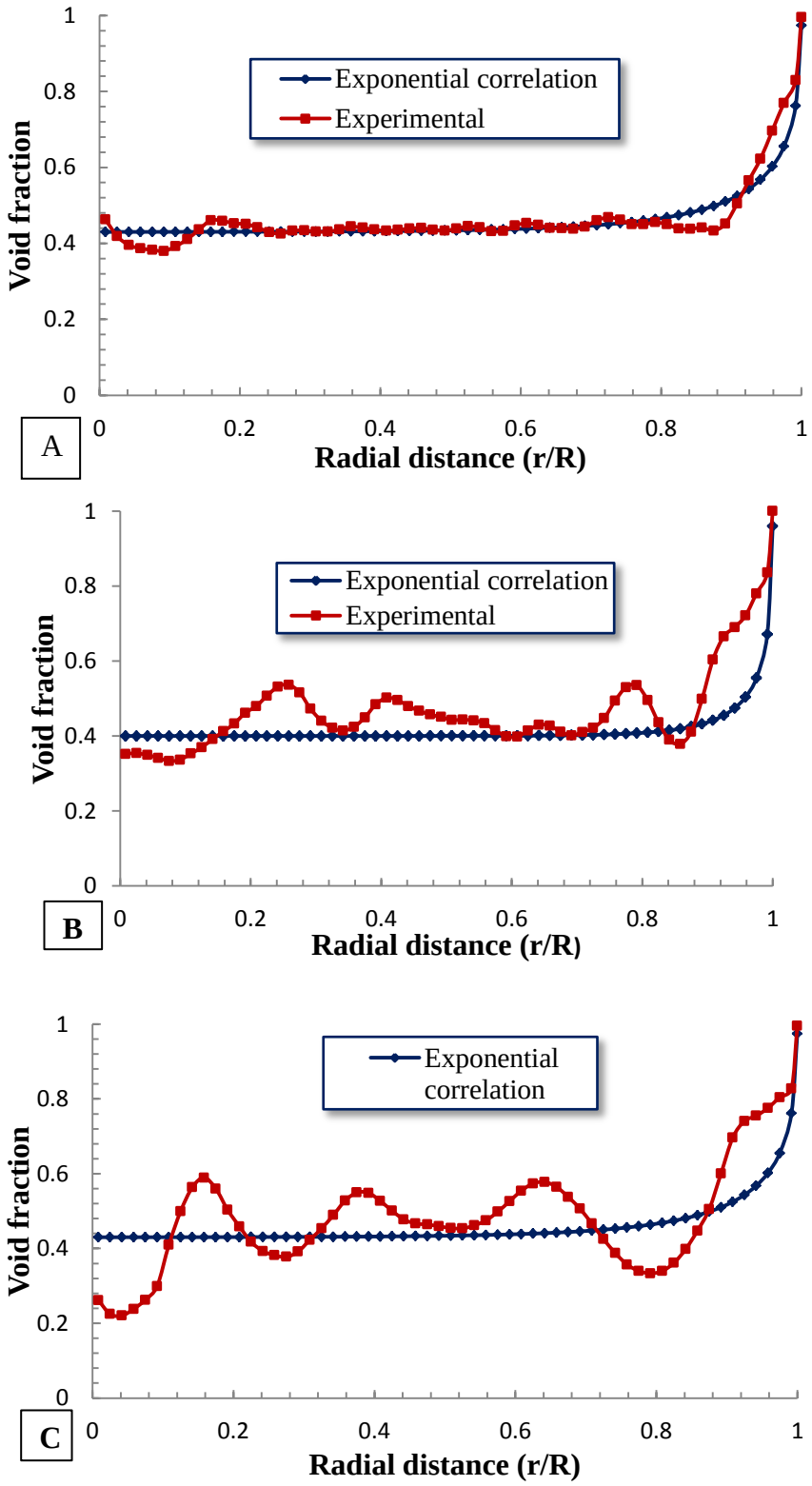

Figure 4.10: A Comparison between the experimental and the exponential correlation of the radial variation in the void fraction for A: D/d = 24, B: D/d = 12 and C: D/d = 6

4.5.3 Radial Void Fraction Profiles: A comparison between Experimental and Correlations Predictions Profiles. Many correlations have been reported for radial void fraction profiles. Both the damping and the oscillatory behavior of the voidage variation were modeled in these expressions. Some of these correlations were, however, still less accurate in predicting the radial void fraction near either the cylinder wall or the cylinder center. Some of these expressions employed more complicated analytical methods to properly predict the radial porosity in the bed. Mueller [56] developed a functional approach to express the axially-averaged radial void fraction variation in a packed bed of spheres. The model was derived based on fundamental geometrical structural principles and is given by the Eq. (24), which is mentioned earlier as:

$$S_n(r) = \pi[R_s^2 - (r - r_s)^2] \qquad for\ R_s \le r_s \le R - R_s\ with\ r_s - R_s \le r \le r_s + R_s$$

This expression was used, along with the Equation (32), to determine the radial void fraction profiles for the three aspect ratios examined in this study (see Figure 4.11). The MATLAB program to calculate the radial profile of void fraction in PBR using Muller (2010) is shown in (Appendix B)**.** The Mueller model [36] provided distribution of the sphere particle centers required to generate the void radial profile. The oscillation behavior of the radial void fraction profile is quite clear in Figure 4.11. The oscillation was large at a smaller aspect ratio (or larger particle size with respect to the bed diameter); it decreased as the aspect ratio increased (smaller particle size with respect to the bed diameter). The damped oscillatory behavior in the radial direction was between a maximum at the wall region and a bulk value in the center. This finding is illustrated more in Figure 4.11 A.

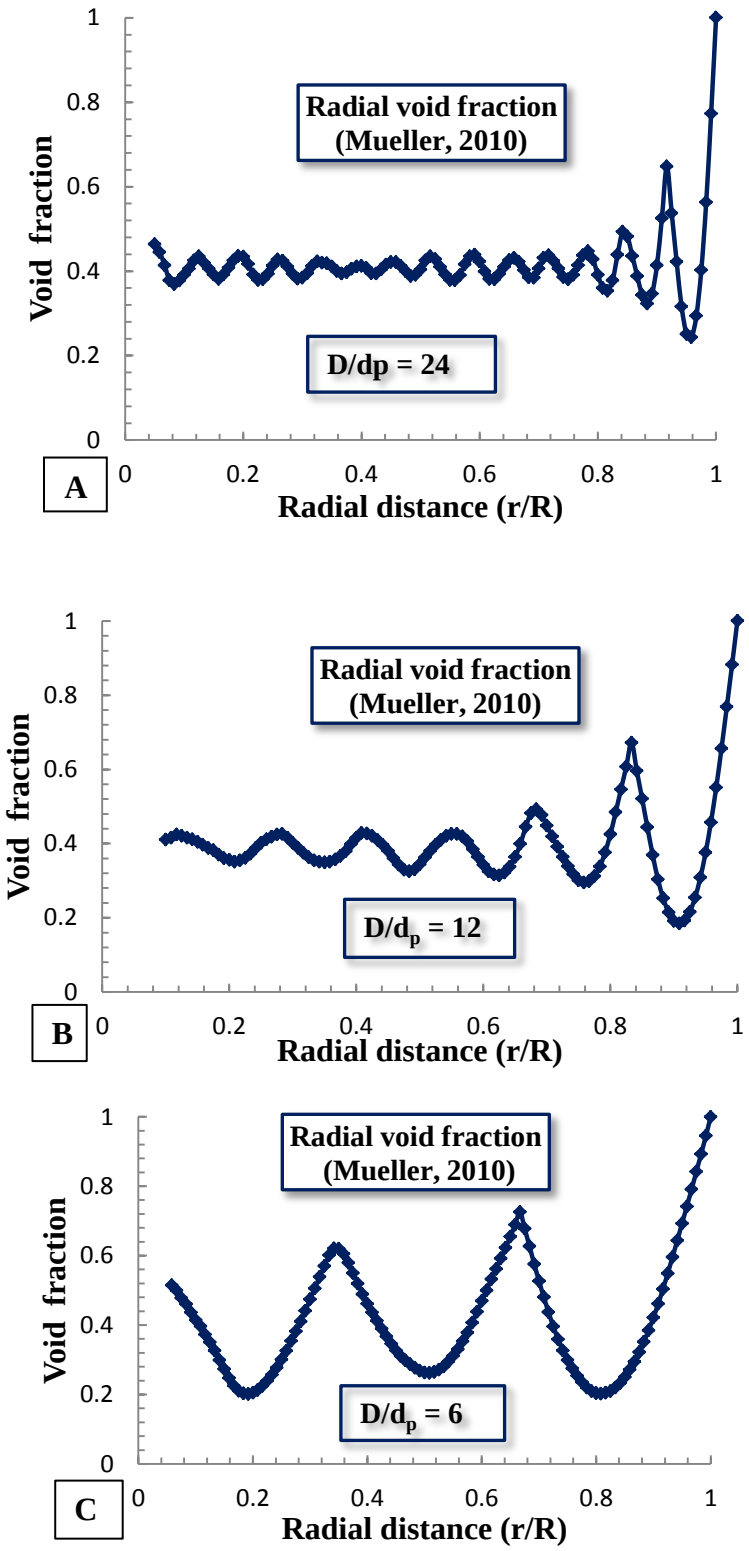

Figure 4.11: Variation in axially averaged radial void fraction model for three aspect ratios of D/d_p: A) 24, B) 12, and C) 6.

The influence of the column to particle diameter ratio on the period of oscillation was also recognized by both Martin [52] and Cohen and Metzner [53]. Mueller [63] presented a simple computer code that can be used to predict the local radial void fraction in sphere packed systems that is based on geometrical principles and analytical approach. It accounts for the radial void fraction in the near and far from the wall regions. This code can also be used to determine the radial void fraction between any two axial positions in the pebble bed. FORTRAN code to calculate the radial porosity (void) (Mueller, 2012) is available in (Appendix C**)**. The comparison between the radial profile of the experimental data of this work using CT, and the prediction of the analytical expression as proposed by Mueller (2012), is illustrated in Figure 4.12. The aspect ratio illustrated in Figure 4.12 was 12 for a three axial levels (3 inches, 6 inches, and 9 inches from the bed base). Despite the damped oscillation behavior for the both measured and predicted profiles, it can be seen that the two profiles exhibit a fluctuation in the data with differences in the amplitude of the oscillation and the shift of the maximum and minimum radial values of the void fraction. These differences are attributed to several factors. First, the radial division (radial increments); (DR) used in the Mueller [63] model (code) was 0.01. This will results in a 600 data points in the output file. The resolution in the CT experiment was 2 mm, which gives a radial increment of 0.28 and a 60 data point in the output file. As a result, data points did not exist in several regions creating deviations. This variance is also ascribed to the packing mode. The actual randomly packing mode is not an easily quantifiable parameter in the mathematical models that are used to predict bed voidage. Moreover, the circumferentially averaged void fraction used to determine the radial variation of void is essentially the average of a square pixel. This average produces results that are less accurate near the wall region (curvature shape). Differences between the experimental and the numerical results could be also attributed to the particles used in the experiments. These particles were not perfectly uniform, as assumed in the model. A comparison between the experimental data and Mueller's (2012) [63] model prediction is illustrated in Figure 4.13 (A: D/d_p=24 and B: D/d_p=6). The radial variation of void fraction at the bulk region (the center cross-section) is illustrated for the aspect ratios of 24 and 6.

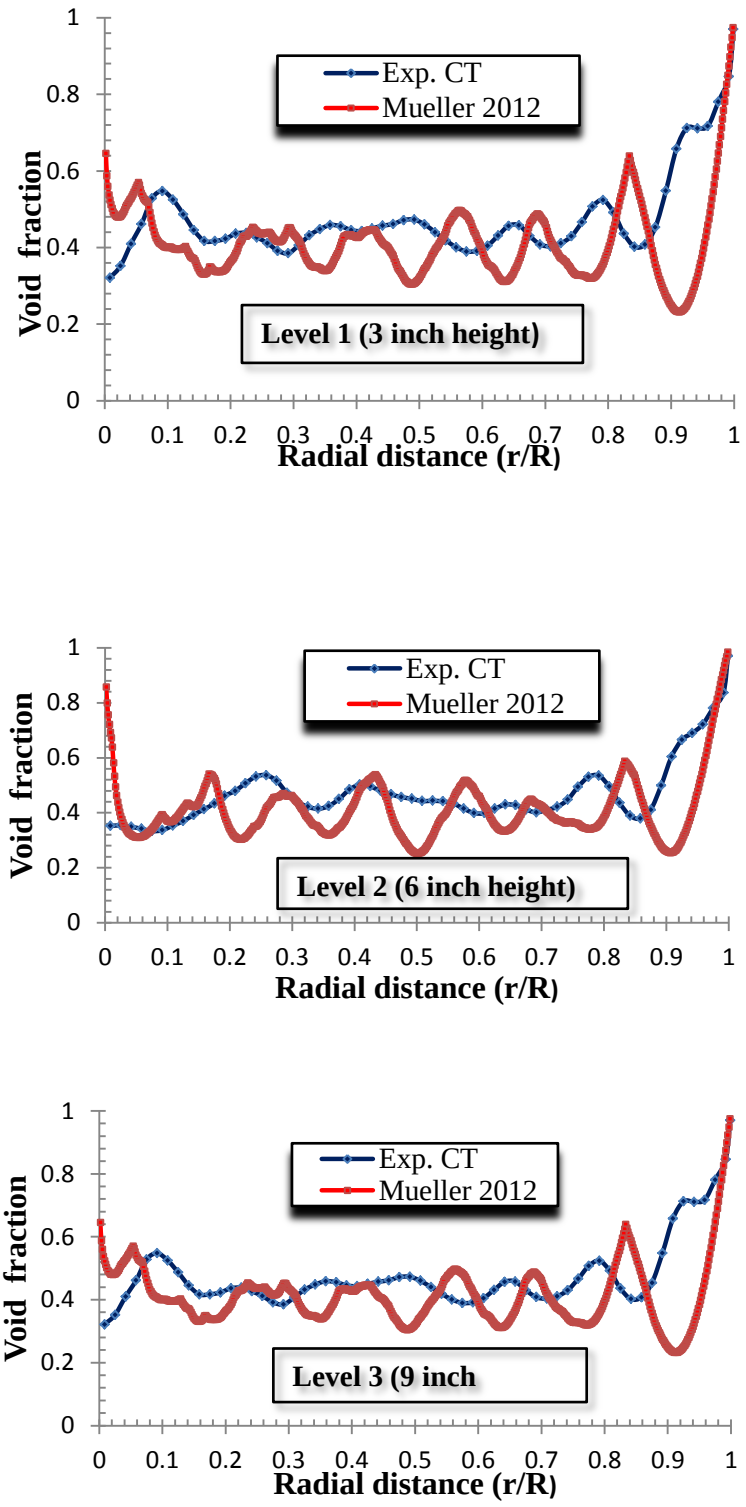

Figure 4.12: Comparison between the experimental radial profile data of this work using CT and the prediction of the analytical expression of Mueller (2012) for the three axial levels (3 inches, 6 inches, and 9 inches from the base of the bed). The aspect ratio (D/d_p) = 12.

The void oscillation behavior near the wall was approximately the same between the experimental and the calculated methods. The results gathered from the CT experiment study and the model had a minimum void fraction at the radial distance of 0.8 (about half pebble diameter); see Figure 4.13 B; they also had different minimum void values (0.34 to 0.14). In the case of the smaller pebble size (half inch) the experimental variation in radial void fraction shows more significant deviation with the numerical data near the wall region (Figure 4.13 A). These results indicate that the influence of the wall-effect on the voidage variation is less pronounced with a large column to particle diameter (e.g., 24).

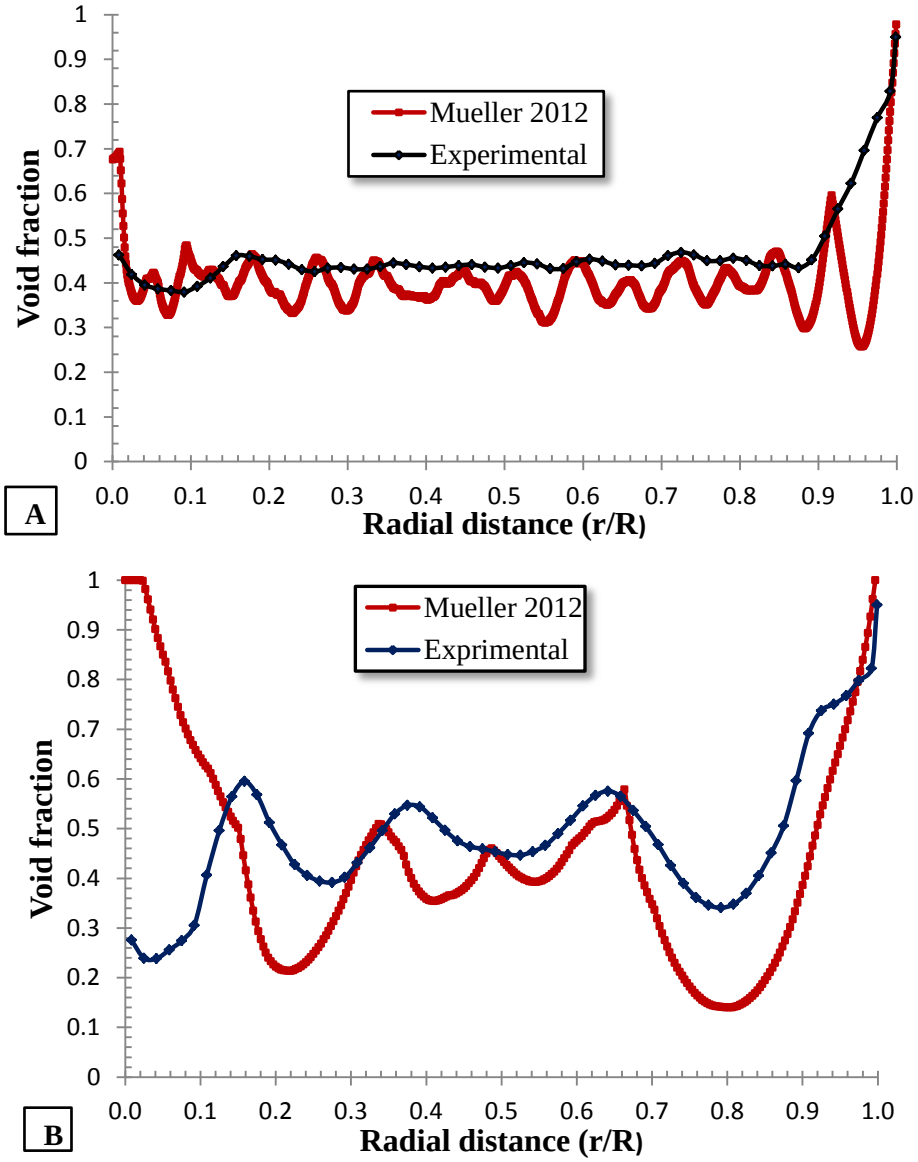

Figure 4.13: A Comparison between CT experimental data and the prediction of the analytical expression of Mueller (2012) radial void fraction profiles at the bulk region for A) aspect ratio (D/d_p) = 24 and B) aspect ratio (D/d_p) = 6

5. REMARKS AND RECOMMENDATIONS

5.1 REMARKS

This work has experimentally investigated for the first time the pebble bed structure in terms of the time averaged voids cross-sectional distribution and radial profiles using high energy-high resolution gamma ray computed tomography (CT). These experiments were successfully conducted to measure the void distribution in a 12-inch diameter packed column using three different sizes of glass spheres (Marbles) 0.5, 1, and 2 inch. Horizontal scans taken at different vertical positions within the packed bed were made for each particle size. The results gathered indicate that the spatial porosity distribution in randomly packed columns is not uniform. Several pockets are always present in the packet beds, where the void is higher than the average value. The void distribution in randomly packed beds is dependent on both the pebble's diameter, compared to the bed diameter, and the packing mode. The bed height did not appear to influence the average porosity. For the circumferentially averaged radial porosity distribution, the void near the center tends to be lower than that in the wall region due to the wall effect and the contacts between pebbles. The radial void fraction's profile exhibited large, dampened oscillations near the wall. The experimental results indicate that the porosity variation can be described by a normal distribution function in the packed bed's bulk region.

Based on the present experimental results of radial void fraction, the comparison with the exponential empirical correlation exhibited a better agreement with higher aspect ratio (small pebbles) than with smaller aspect ratio (large pebbles).

5.2 RECOMMENDATIONS

Measurements of void and solid fraction distributions have already been performed successfully with DSCT scanner facility. Since the gamma source has a Poisson distribution, further experiments using a strong gamma source will allow us to reduce the measurement time, increase the accuracy of the data and decrease the width of the collimator giving us a finer grid of measurement points (increase the resolution of measurements).

Two CT scans must be performed in this study to measure the cross-sectional phase distribution. These scans were for air only to obtain (I_0) and packed bed to obtain (I). The attenuation of gamma rays at the column wall decreased the value of void fractions near the wall. It is, therefore, better to have a third CT scan with an empty column. The attenuation made by the column wall should then be subtracted from the packed bed measurements.

Mueller [56] generated pebble beds at different bed size and spheres sizes. Suitable codes are available to calculate the radial local void fraction. The authors hope that with enough set of data, one can develop the needed correlations such as the mean, variance and radial profiles that assist in properly generate the bed structure as an input to CFD to simulate the flow of solids and gas in the pebble beds.

Further experiments should include measurements of the axial void fraction profiles with finer cross sectional scans to increase the data points and thus obtain more accurate results.

In further works, different types of pebbles need be used (graphite with 6 cm diameter and large bed diameter to obtain $D/d_p > 25$) to simulate properly the pebble bed reactor. Experiments should also be conducted with different packing modes (very loose packing, poured random packing, and dense packing). Also, it is important to examine how the bed structure varies with the moving pebbles. This can be done by performing CT when the pebble is moving downward using the newly developed cold flow solids experiment.

APPENDIX A

Program to describe the histogram of void and solids fractions

```
% program describes the histogram plotting
% Missouri S&T, Dept of Nuclear Engineering
clc
clear all
close all
%I= textread('void_D2L2.txt','%f'); % take the input from Notepad
load void_D2L2.mat
ind= find(I==1);
I(ind)=[]; % voidage
V = var(I)
M = mean(I)
x=min(I):.05:max(I); % Select the range what you desire
figure, hist(I,x); % show histogram
title('voidage')
xlabel('x')
ylabel('y')
grid on
% I=1-I;% for solid
% ridV = var(I)
% M = mean(I)
% x=min(I):.05:max(I); % Select the range what you desire
% figure, hist(I,x); % show histogram
% title('solid')
% xlabel('x')
% ylabel('y')
% g on
%xlswrite('solid_holdup1.xls',I);
```

APPENDIX B

Program to calculate the radial profile of void in PBR

```
This program is to calculate the radial profile of void
% in pebble bed reactor using Mueller 2010 correlations
clc
clear all
close all
Rs= 0.25;
h= 12;
num= xlsread('Prof_12_05_12.xlsx');
X= num(1:end,1);
Y= num(1:end,2);

rs= sqrt(X.^2+Y.^2);
Rc=6.0;
i=1;
for r= 0.0:0.05:6.0
    Sn=0;
    for j=1:12077
        if rs(j)<Rs
            if r<=(rs(j)+Rs) && r>(Rs-rs(j))
                Sn=Sn+pi*((Rs^2-(r-rs(j)).^2));
            elseif r<(Rs-rs(j))
                if r<=rs(j)
                    Sn=Sn+ 2*pi*r*((Rs.^2-(r+rs(j)).^2).^(1/2)+(Rs.^2-
(r-rs(j)).^2).^(1/2));
                elseif r>rs(j)
                    Sn=Sn+ 0.5*pi*r*(3*(Rs^2-
(r+rs(j)).^2).^(1/2)+2*(Rs^2-(r-rs(j)).^2).^(1/2)+3*(Rs^2-
rs(j).^2).^(1/2));
                end
            end
        end
        if rs(j)>=Rs %&& rs(j)<=(Rc-Rs)
            if r>=(rs(j)-Rs) && r<=(rs(j)+Rs)
                Sn=  Sn+pi*((Rs^2-(r-rs(j)).^2));
            end
        end
    end
```

```
    sum(i,1)=r;
    sum(i,2)= 1-Sn/(2*pi*r*h);
    i=i+1;
end

plot(sum(:,1),sum(:,2));
oid=fopen('void5.txt','w');
fprintf(oid, '%10.3f\t %10.3f\n',sum');
fclose(oid);
```

APPENDIX C

FORTRAN Program to calculate the radial porosity (Mueller 2012)

```
IMPLICIT REAL(A-H,O-Z),INTEGER(I-N)
      DIMENSION XC(100000),YC(100000),ZC(100000),POR(100000),RBN(100000)
      PARAMETER (DR=0.01,DZ=0.01,F1=0.0,F2=1.0, PI=3.141592653589)
      OPEN(UNIT=5, FILE='solid_D3L12.DAT')
      OPEN(UNIT=6, FILE='void_D3L12.DAT')
      READ(5,*) DB,DS,HB,NOP
      READ(5,*) (XC(I),YC(I),ZC(I),I=1,NOP)
      NR = 0
      NZ = 0
      PORZ = 0.0
      Z = HB*F1
      R = DS*DR
5     ARCS = 0.0
      DO 10, I = 1,NOP
      IF (Z.LT.ZC(I)-DS/2.0.OR.Z.GT.ZC(I)+DS/2.0) GO TO 10
      RP = SQRT(XC(I)**2+YC(I)**2)
      RZ = SQRT((DS/2.0)**2-(ABS(ZC(I)-Z))**2)
      IF (R.LT.RP-RZ.OR.R.GT.RP+RZ) GO TO 10
      IF (R.LE.RZ.AND.RP.EQ.0.OR.R+RP.LE.RZ.AND.RP.LT.RZ) THEN
       ARC = 2*PI*R
       GO TO 15
      END IF
      IF ((RP**2+R**2-RZ**2)/(2.0*R*RP).GE.1) GO TO 10
      ARC = 2.0*R*ACOS((RP**2+R**2-RZ**2)/(2.0*R*RP))
```

```
15    ARCS = ARCS + ARC
10    CONTINUE
      PORZ = PORZ+1.0-ARCS/(2.0*PI*R)
      Z = Z+DS*DZ
      NZ = NZ+1
      IF (Z.LT.HB*F2) GO TO 5
      NR = NR+1
      POR(NR) = PORZ/NZ
      RBN(NR) = R/(DB/2.0)
      R = R+DS*DR
      Z = HB*F1
      NZ = 0
      PORZ = 0.0
      IF (R.LT.(DB/2.0)) GO TO 5
      WRITE (6,*)((1.0-RBN(NR-I+1))*DB/(2.0*DS),POR(NR-I+1),I,I=1,NR)
      END
```

REFERENCES

1. Boer B., 2008."Optimized core design and fuel management of a pebble-bed type Nuclear Reactor". IOS Press. ISBN 978-1-58603-966-0.

2. International Atomic Energy Agency. Nuclear power reactions in the world. Technical report IAEA-RDS-2/28, Vienna, Austria, July 2008. ISBN 978-92-0-107708-0.

3. GEN IV International Forum, 2007 Annual Report. Site web: www.gen-4.org. Last accessed, November 2014.

4. Letcher T. M., 2008. Future energy improved sustainable and clean options for our planet. Part III "Potentially important new types of energy", Elsevier.

5. Forsberg C. W. and Moses D. L., 2009. Safeguards challenges for pebble-bed reactors designed by People's Republic of china. Global nuclear security technology division. ORNL/TM-2008/229.

6. Enformable Nuclear News. Lucas W. Hixson. Site web: http://enformable.com. Last accessed, April 2013.

7. Banzant M. (2006): Modeling and simulation of granular flow in pebble bed nuclear reactor. Report to the department of energy, office of advanced scientific computer research.

8. Lee N. Y., Jung S. H., and Kim J. B. (2009): Evaluation of the measurement geometries and data processing algorithms for industrial gamma tomography technology. Applied radiation and isotopes, 67, 1441-1444.

9. Aboulwafa M. and Kendall E. (1980): The measurement of component ratios in multiphase systems using gamma ray attenuation, J. Phys. E: Sci Instrum., 13, 341-345.

10. Harrison M. (1990): Gamma scan evaluation for distillation column debottlenecking, Chem. Eng. Progress, 86, 37-44.

11. Bowman J. (1993): Use column scanning for predictive maintenance. Chem. Eng. Progress, 89, 34-41.

12. Kumar S. (1994). Computed tomographic measurements of void fraction and modeling of the flow in bubble columns [PhD Thesis]: Florida Atlantic University

13. Kumar S., Moslemian D., and Dudukovic M. (1997): Gas-holdup measurements in bubble columns using computed tomography. AIChE Journal, 43(6):1414-1425.

14. Chaouki, J., Larachi, F., Dudukovic, M. P. (1997): Noninvasive tomographic and velocimetric monitoring of multiphase flows. Industrial & Engineering Chemistry Research, 36 (11), 4476-4503.

15. Roy S. (2000): Quantification of two phase flow in liquid-solid risers. D.Sc. Thesis, Washington University, St Louis, MO.

16. Chen, J., N. Rados, M. H. Al-Dahhan, M. P. Dudukovic, D. Nguyen and K. Parimi (2001): Particle motion in packed/ ebullated beds by CT and CARPT. AIChE Journal, 47(5): 994-1004.

17. Wang Z., Afacan A., Nandakumar K., Chuang K., (2001): Porosity distribution in random packed columns by gamma ray tomography. Chem. Eng. And Process, 40, 209-219.

18. Rados N. (2003): Slurry bubble column hydrodynamics. D.Sc. Thesis, Washington University, St. Louis, MO.

19. Roy S., Kemoun A., Al-Dahhan M., Dudukovic M., Skourlis T., Dautzenberg F. (2004): Countercurrent flow distribution in structured packing via computed tomography. Chemical Engineering and Processing 44(1):59-69.

20. Rados N., Shaikh A., Al-Dahhan M. (2005): Phase distribution in a high pressure slurry bubble column via a single source computed tomography. The Canadian Journal of Chemical Engineering, 83:104-112.

21. Hampel U., Bieberle A., Hoppe D., Kronenberg J., Schlecher E., Suhnel T., Zimmermann F., Zippe C. (2007): High resolution gamma ray tomography scanner for flow measurements and non-destructive testing applications. Review of Scientific Instruments 78, 103704.

22. Varma R., (2008): Characterization of anaerobic bioreactors for bio-energy generation using a novel tomography technique. D.Sc. thesis, Washington University, St. Louis, MO.

23. Vasquez P., Mesquita C., LeRoux G., Hamada M. (2010): Methodological analysis of gamma tomography system for large random packed columns. Appl. Rad. and Isotopes, 68, 658-661.

24. Almesfer M., Ahmed F., Neogi P., and Al-Dahhan M. (2012): Effect of internals on gas holdup in bubble columns using computed Tomography (CT). 6th International symposium on process tomography.

25. Ahmed F., Almesfer M., and Al-Dahhan M. (2012): Bed structure characterization of pebble bed reactor using Gamma-Ray Tomography. 6th International symposium on process tomography.

26. Dijk V. (2008): Radial void fraction measurement of randomly packed pebble bed. Thesis, Delft University of Technology, Delft, Netherlands.

27. Auwerda G., Kloosterman J., Winkelman A., Groen J., Dijk V. (2010): Comparison of experiments and calculations of void fraction distributions in randomly stacked pebble beds. Advan. Phys. To power the Nuc. Renaissance, Pittsburg, Pennsylvania, U.S.A.

28. Chris H., Gary S., James W., and Martin Z. (2006): Analysis of granular flow in a pebble-bed nuclear reactor. Phys. Rev. E 74, Issue 2.

29. Toit G. G., (2008): Radial variation in porosity in annular packed beds. Nuc. Eng. & Design, 238, 3037-3079.

30. Cogliati J. and Ougouag A. (2006): Pebbles: A computer code for modeling packing, flow and re-circulation of pebbles in a pebble bed reactor. 3rd International tropical meeting on high temperature reactor technology, Proceedings HTR2006, Johannesburg, South Africa.

31. Zhang w., Thompson K., Reed A., and Beenken L. (2006): Relationship between packing structure and porosity in fixed beds of equilateral cylindrical particles. Che. Eng Sci., 61, 8060-8074.

32. Roblee L. H., Baird R. M. and Tierney J. W. (1958): Radial porosity variations in packed beds. AIChE Journal, 4, pp. 460-464.

33. Benenati R. F. and Brosilow C. B. (1962): Void fraction distribution in beds of spheres. AIChE Journal, 8, pp. 359-361.

34. Goodling J., Vachon R., Stelpflug W. and Ying S. (1983): Radial porosity distribution in cylindrical beds packed with spheres. Powder Technology, 35, pp. 23-29.

35. Kufner R. and Hofman H. (1990): Implementation of radial porosity and velocity distribution in a reactor model for heterogeneous catalytic gas phase reactors. Chem. Eng. Sci, Vol. 45, No. 8, pp. 2141-2146.

36. Mueller G. (1992): Radial void fraction distributions in randomly packed fixed beds of uniformly sized Spheres in cylindrical containers. Powder Technology, 72, pp. 269-275.

37. Niu M., Akiyama T., Takahashi R. and Yagi J. (1996): Reduction of the wall effect in a packed bed by hemispherical lining. AIChE Journal, 42, pp. 1181-1186.

38. Sederman A., Alexander P. and Gladden L. (2001): Structure of packed beds probed by magnetic resonance imaging. Powder Technology, 117, pp. 255-269.

39. Hassan A. Y. and Dominguez-Ontiveros E. E. (2008): Flow visualization in a pebble bed reactor experiment using PIV and refractive index matching techniques. Nuc. Eng. & Design, 238, 3080-3085.

40. Mariani N., Salvat W., Campesi A., Barreto G. and Martinez (2009): Evaluation of structural properties of cylindrical packed beds using numerical simulations and tomography experiments. International Journal of Chemical Reactor Engineering, Vol. 7, Article A82

41. Jeschar J. (1964): Pressure drop in a packed bed of spheres. Archive for the iron and steel industry, 35, 91-108.

42. Kugeler K. and Schulten R. (1989): High temperature reactor technology, Springer Verlag, 1989.

43. Dixon A. G. (1988): Correlations for wall and particle shape effects on fixed bed bulk voidage. Candian J. Chem. Eng., 66, 705-708.

44. Theuerkaut J., Witt P. and Schwesing D. (2008): Analysis of particle porosity distribution in fixed beds using the discrete element method. Powder Tech., 165, 92-99.

45. De Klerk, A. (2003). Voidage variation in packed beds at small column to particle diameter ratios. AICheJ, 49, No. 8, 2022 – 2029.

46. Pushnov A. S. (2006): Calculations of average bed porosity. Chem. Petro. Eng. Vol. 24, Nos. 1-2

47. Zou R.P. and Yu, A.B. (1995). The packing of spheres in a cylindrical container: the thickness effect. Chem.Eng.Sci. 50, 1504 – 1507.

48. Sodre J. R and Parise J. A. R. (1998): Fluid flow pressure drop through an annular bed of spheres with wall effects. Exp. Therm. Fluid Sci., 17, 265-275.

49. Rbeiro A. M., Neto P. and Pinho C. (2010): Mean porosity and pressure drop measurements in packed beds of monosized spheres: Side wall effects. Int. Rev. Chem. Eng., Vol. 2, N.1, 40-46.

50. Toit G. G., (2002): The pebble-bed reactor: effect of wall channeling on the flow in the core, Kruger Park, South Africa.

51. White D. M., Tien C. L. and ToiT G. G., (1978): Analysis of flow channeling near the wall in packed beds, Warme- und Stoffubertragung, Vol. 21, pp. 291-296.

52. Martin H. (1978): Low peclet number particle to fluid heat and mass transfer in packed beds. Chem. Eng. Sci. 33, 913-919.

53. Cohen Y. and Metzner B. (1981): Wall effects in laminar flow of fluids through packed beds. AICHE J. Vol. 27, No.5, 705-715.

54. Vortmeyer D. and Schuster J., (1983): Evaluation of steady flow profiles in rectangular and circular packed beds by variation method. Chem. Eng. Sci. 38, 1691-1699.

55. Cheng P. and Hsu C. T. (1986): Fully developed, force convective flow through an annual packed-sphere bed with wall effects. Int. J. Heat Mass Trans. 29, 1843-1853.

56. Mueller G. E., (2010): Radial porosity in packed beds of spheres. Powder Technol., 203, 626-633.

57. Toit Du G. (2002): The numerical determination of the variation in the porosity of the pebble bed reactor core. Proc. Int. Topl. Mtg. high temperature reactor technology, Petten, Netherlands.

58. Salvat W. I., Mariani N. J., Barreto G. F. and Martinez O. M. (2005): An algorithm to simulate packing structure in cylindrical containers. Catal. Today, 513-519.

59. Cogliati J. J. and Ougouag A. M. (2006): Pebble: A computer code for modeling packing, flow and re-circulation of pebbles in a pebble bed reactor. HTR2006, 3rd Int. Top. Mtg. on high temp. Reactor tech, Johannesburg, South-Africa.

60. Rycroft C. H. et al. (2006): Analysis of annular flow in pebble bed reactor. Physical Review E, 74.

61. Kloosterman J. L. and Ougouag A. M (2007): Comparison and extension of Dancoff Factors for pebble bed reactors. Nuc. Sci. Eng., 157, 16-29.

62. Pieritz R. A. P., Reimann J. and Ferrero C. (2011): Tomography analysis of the inner structure of pebbles and pebble beds. Adv. Eng. Mat. 13, No.3, 145-155.

63. Mueller G. (2012): A simple method for determining sphere packed bed radial porosity. Powder Tech., 229, 90-96.

64. Khane V. (2014): Experimental and computational investigation of flow of pebbles in apebble bed nuclear reactor. D.Sc. thesis, Missouri University of Science and Technology, Rolla, MO.

65. Kak A, Stanley M, (2001) Principles of Computerized Tomographic Imaging, Society for industrial and applied mathematics (SIAM), first published by IEEE press, New York (1988).

66. Peter Blum, Ocean Drilling Program (1997): Physical Properties Handbook: A Guide to the Shipboard Measurement of Physical Properties, Texas A&M University.

67. The Lund/LBNL Nuclear Data Search (1999): Table of radioactive isotopes

68. Lee N., Jung S., and Kim J. (2009): Evaluation of the measurement geometries and data processing algorithms for industrial gamma tomography technology. Appl. Rad. and isotopes, 67, 1441-1444.

69. Lange K. and Carson R, 1984: EM reconstruction algorithms for emission and transmission tomography, J. Comput. Assist. Tomogr., 8, 306–16.

70. Dempster, A., Laird N., and Rubin D. (1977): Maximum Likelihood from Incomplete Data via EM Algorithm. J. Roy Stat Soc, B 39: 1.

71. O'Sullivan J. A. and Benac J. 2007: Alternating minimization algorithms for transmission tomography IEEE Trans. Med.Imaging 26 283–97

72. Varma R., O'Sullivan J., and Al-Dahhan M. (2007): Application of Alternating - Minimization (AM) in dual source gamma ray computer tomography for imaging three phase systems. 5th World Congress on Industrial Process Tomography, Bergen, Norway.

73. Varma V., Bhusarapu R., O'Sullivan J., and Al-Dahhan M. (2007): A comparison of alternating minimization and expectation maximization algorithms for single source gamma ray tomography, Meas. Sci. Technol., 18, 1–13.

74. Saint-Gobain (2004): Efficiency calculations for selected scintillators Saint-Gobain Crystals. Web, (http://www.detectors.saint-gobain.com/) p. 16.

75. Vesvikar MS. (2006): Understanding the hydrodynamics of anaerobic digesters for bioenerg production [D.Sc.]: Washington University-St. Louis

76. Romeu A. P., Jorg R. and Claudio F. (2011): Tomography analysis of the inner structure of pebbles and pebble beds. Adv. Eng. Mat. 13, No.3, 145-155.

VITA

Fadha Shakir Ahmed was born in Baghdad, Iraq. After completing his Baccalaureate at Al Kundy High-School in Baghdad in 1980, Fadha entered Al Mustansiriya University in Baghdad, Iraq. He received a Bachelor degree of Science with a major in physics in 1984During the following ten years; he was employed as a Health Physicist in the Iraqi Atomic Energy commission in Baghdad. Fadha entered the Graduate School of Al Mustansiriya University in Baghdad in 1997. He gained his Master Degree in Physics of Science. In August 2001, he entered the Graduate school of Nanjing University, Nanjing, Jiangsu province, China. He received his PhD Degree of Science in Physics from Nanjing University in 2005. He worked as a scholar associate in Washington University in St. Louis from 2005 to 2009. He worked as a Research Associate visitor at Missouri S&T from 2010-212. During this time, he attended the Master program of Nuclear Engineering in Missouri S&T in 2011. Fadha received his Master in the Nuclear Engineering from Missouri University of Science and Technology in December, 2014.